

# Enhanced Photocatalytic Degradation of Tetracycline-Class Pollutants in Water Using a Dendritic Mesoporous Silica Nanocomposite Modified with UiO-66

Fatemeh Deymeh<sup>1,2</sup>, Ali Ahmadpour<sup>1,2,\*</sup>, Ali Allahresani<sup>3</sup>, Arash Arami-Niya<sup>4,\*</sup>

<sup>1</sup>Department of Chemical Engineering, Faculty of Engineering, Ferdowsi University of Mashhad, P.O. Box 91779-48944, Mashhad, Iran.

<sup>2</sup>Industrial Catalysts, Adsorbents and Environment Lab., Oil and Gas Research Institute, Ferdowsi University of Mashhad, P.O. Box 91779-48974, Mashhad, Iran.

<sup>3</sup>Department of Chemistry, College of Sciences, University of Birjand, P.O. Box 97175-615, Birjand, Iran.

<sup>4</sup>Discipline of Chemical Engineering, Western Australian School of Mines: Minerals, Energy and Chemical Engineering, Curtin University, GPO Box U1987, Perth, WA 6845, Australia.

## Abstract

Tetracyclines, a widely used group of antibiotics in agriculture and animal husbandry, are causing water pollution and the emergence of antibiotic-resistance genes. This study reports the synthesis of a metal-organic framework nanocomposite of UiO-66 based on modified dendritic fibrous nano-silica to act as a photocatalyst for the degradation of doxycycline (DOX) and tetracycline (TTC) as drug model pollutants in water. This nanocomposite demonstrated about three times better photodegradation performance than UiO-66 due to a decreased electron-hole recombination rate, increased conductivity, and decreased band gap, leading to higher pollutants reduction efficiency. Structural and morphological analyses were performed on the nanocomposite, and various influencing parameters, including sample pH, catalyst dose, and irradiation time, were studied on the photocatalytic degradation of DOX and TTC to optimise the photodegradation process. At the optimum condition, the maximum photodegradation of  $97.2 \pm 3.1\%$  was achieved for solutions containing  $200 \text{ mg.L}^{-1}$  of each drug. The results showed that the proposed photocatalyst is stable and effective in eliminating tetracycline-class pollutants from water and wastewater, with high efficiency and fast kinetics. The reusability of the catalyst was examined, and no significant decrease in the efficiency of the catalyst was observed after five times.

**Keywords:** Tetracycline-class pollutants, Photodegradation, Metal-organic framework, UiO-66, DFNS.

---

\* Corresponding author. Tel: +98-51-38805006. Email: [Ahmadpour@um.ac.ir](mailto:Ahmadpour@um.ac.ir)

\* Corresponding author. Tel: +61-8-9266-5482. Email: [Arash.araminiya@curtin.edu.au](mailto:Arash.araminiya@curtin.edu.au)

## 31 **1. Introduction**

32 The issue of water pollution has raised significant concern globally due to the presence of harmful  
33 substances like heavy metal ions,<sup>1-4</sup> anions,<sup>5,6</sup> antibiotics,<sup>7</sup> and dyes,<sup>8,9</sup>. The rapid development of  
34 industrialisation has led to an increase in the quantity of these contaminants, posing substantial  
35 risks to both human health and the environment. Particularly, antibiotics, extensively used in  
36 modern medicine for an extended period, are now pervasive in the environment.<sup>10</sup> As these  
37 antibiotic compounds disperse and persist in the environment, they contribute to antibiotic  
38 residues, which poses a serious threat to human and ecosystem health. In recent years, the  
39 management of antibiotic contaminants in water and possible treatment methods has become a  
40 popular topic of discussion Addressing this issue is crucial to safeguarding the well-being of both  
41 human populations and the delicate balance of natural ecosystems.

42 Doxycycline (DOX) and tetracycline (TTC) are two kinds of Tetracyclines that are among the  
43 largest groups of antibiotics widely used in agriculture and as growth promoters in livestock  
44 farming, leading to water pollution and the emergence of antibiotic resistance genes.<sup>11</sup> A variety  
45 of methods, including sedimentation,<sup>12</sup> ion exchange,<sup>13</sup> reverse osmosis,<sup>14,15</sup> electrochemistry,<sup>16,17</sup>  
46 membrane separation,<sup>18</sup> photodegradation,<sup>19-24</sup> biodegradation<sup>25</sup> and adsorption<sup>7</sup> have been  
47 employed for the treatment of wastewater containing DOX and TTC. Among them, adsorption and  
48 photodegradation are the most proper approaches for isolating these TTC-class pollutants from  
49 water resources.<sup>10,26</sup> However, in the adsorption method, the adsorbents will be contaminated after  
50 the process, and various integration schemes are needed to isolate TTC-class pollutants effectively.

51 Heterogeneous catalytic photodegradation is a low-cost and efficient approach for the degradation  
52 of different contaminants with safe derivatives (such as CO<sub>2</sub>, H<sub>2</sub>O, etc.).<sup>10</sup> The method is based on  
53 the absorption of photons with energy levels equal to or greater than the energy of the catalytic  
54 band gap.<sup>10</sup> After the catalyst absorbs energy, the valence band electrons (e<sup>-</sup>) move to the  
55 conduction band, generating photogenic pores (h<sup>+</sup>) in the valence band.<sup>10</sup> It oxidises water  
56 molecules to produce hydroxyl radical (•OH) and superoxide radical anions (•O<sub>2</sub><sup>-</sup>), which is an  
57 effective oxidant in the water environment. Ultimately, the generated •OH radicals can oxidatively  
58 degrade numerous organic compounds, including DOX and TTC antibiotics.<sup>10,27</sup>

59 Metal-organic frameworks (MOFs), known as coordination polymer particles and nano-hybrid  
60 materials, have been developed as effective photocatalysts and they have different applications for

61 example water splitting, CO<sub>2</sub> reduction, organic conversion reactions, and decomposition of  
62 pollutants.<sup>28–30</sup> MOFs' high structural and compositional diversity make them attractive candidates  
63 for different applications.<sup>28–34</sup> The use of MOF-based hybrids in photodegradation applications has  
64 been extensively reported in recent years.<sup>35–40</sup> A variety of MOFs shell–core nanomaterials have  
65 been recently prepared to make uniform spherical MOF nanocomposites by nucleating and  
66 growing MOFs on carboxylate or hydroxylate-modified substrates, such as silica,<sup>41</sup> polystyrene,<sup>42</sup>  
67 Fe<sub>3</sub>O<sub>4</sub>,<sup>43</sup> Al<sub>2</sub>O<sub>3</sub><sup>44</sup> and so on. Zirconium-based MOFs such as UiO-66, commonly known for being  
68 fabricated of hexagonal zirconium clusters bound to terephthalate ligands,<sup>45,46</sup> were introduced as  
69 porous structures with high photocatalytic activity mainly due to their abundant active sites,  
70 extending light absorption, and effectively separating photogenerated carriers.<sup>29,36,38</sup>

71 MOFs combined with silica might improve the colloidal stability of MOFs, resulting in a decrease  
72 in their biodegradability.<sup>47</sup> In this regard, mesoporous fibrous nano-silica (DFNS), with unique  
73 properties and microsphere-like morphology, has been reported as effective and excellent catalyst  
74 support compared to conventional mesoporous silica materials due to its high accessible surface  
75 area and constant porosity.<sup>48</sup> Nevertheless, in light of DFNS's neutral structure, surface  
76 modification becomes imperative to enhance its adsorptive and catalytic capabilities.<sup>49,50</sup> So far,  
77 various elemental, organic, and semiconductor materials, such as Ag, Al, Au, TiO<sub>2</sub>, Fe<sub>3</sub>O<sub>4</sub>/SiO<sub>2</sub>,  
78 and chitosan-oleic acid, have been employed for surface modification of DFNS.<sup>49</sup>

79 This study aimed to investigate the feasibility of nucleation and growth of UiO-66 on the surface  
80 of amine-modified DFNS to develop an advanced hetero-structured photocatalyst for the  
81 photodegradation of DOX and TTC under UV light. Through the synthesis of UiO-66@NH<sub>2</sub>-  
82 DFNS nanocomposites, the ordered microporosity of UiO-66 MOF and the mesoporosity of DFNS  
83 can be combined. The success of the proposed UiO-66@NH<sub>2</sub>-DFNS synthesis was investigated,  
84 and its potential was evaluated for the photodegradation of DOX and TTC contaminants from  
85 aqueous media. The effects of various variables, including sample pH, catalyst dose, and  
86 irradiation time, on the photocatalytic degradation of DOX and TTC were analysed using response  
87 surface methodology. Additionally, the photodegradation mechanism of DOX and TTC was  
88 investigated to enhance the photocatalytic performance of UiO-66@NH<sub>2</sub>-DFNS.

## 89 2. Materials and Methods

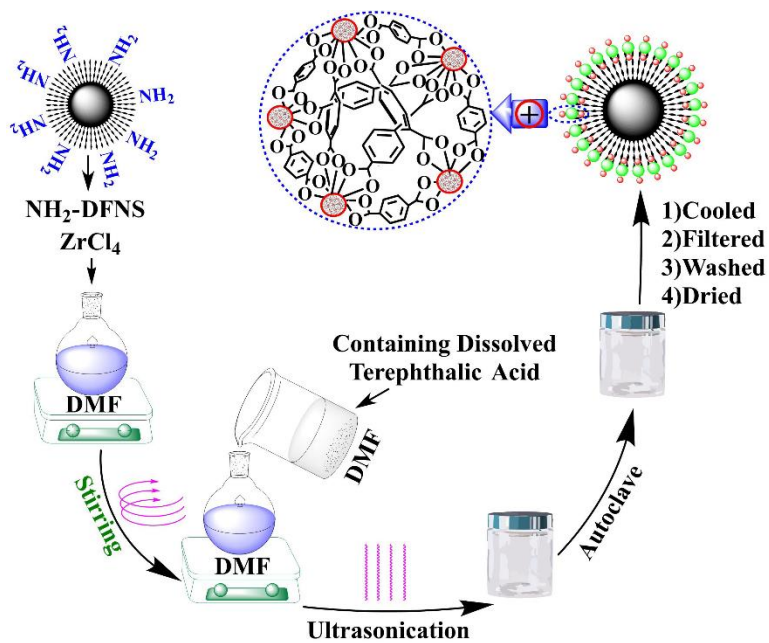
### 90 2.1. Chemicals

91 Cetyltrimethylammonium bromide (CTAB,  $C_{19}H_{42}BrN$ ), urea ( $CH_4N_2O$ ), 3-aminopropyl tri-  
92 ethoxy silane (APTES,  $C_9H_{23}NO_3Si$ ), tetraethyl orthosilicate (TEOS,  $SiC_8H_{20}O_4$ ), zirconium  
93 tetrachloride ( $ZrCl_4$ ), 1,4-benzenedicarboxylic acid (Terephthalic acid,  $C_8H_6O_4$ ), N, N-dimethyl  
94 formamide (DMF,  $C_3H_7NO$ ), chloroform ( $CHCl_3$ ), cyclohexane ( $C_6H_{12}$ ), 1-pentanol ( $C_5H_{11}OH$ )  
95 and ethanol ( $C_2H_6O$ ) of analytical and synthesis grades were procured from Merck Co. (Germany).  
96 DOX and TTC, both with a purity of at least 98%, were acquired from Sigma-Aldrich Co. (USA).  
97 The solutions were freshly prepared each day using double-distilled water (DDW). The pH of the  
98 prepared solutions was adjusted using hydrochloric acid and sodium hydroxide solutions (1.0 M)  
99 sourced from Merck (Germany).

### 100 2.2. Synthesis of UiO-66@NH<sub>2</sub>-DFNS

101 The DFNS sample was prepared using the hydrothermal approach.<sup>48,51</sup> The method of compound  
102 synthesis is described in Deymeh et al.<sup>24</sup> UiO-66 was synthesised through a solvothermal  
103 method.<sup>29</sup> Initially, a 100 mL Schott bottle was filled with 10 mL of DMF, followed by the  
104 dissolution of 0.7 g terephthalic acid and 0.5 g  $ZrCl_4$  at 80°C for 30 minutes. The solution was  
105 clarified in an ultrasonic bath and then transferred to a stainless-steel Teflon-lined autoclave, which  
106 was placed in an oven at 120°C for 24 hours. After cooling, the sample underwent three  
107 centrifugation cycles with DMF to eliminate any residual reactants, followed by additional cycles  
108 with absolute methanol to remove DMF. The resulting powder was soaked in fresh DMF for 1  
109 hour and in methanol for 24 hours, and subsequently vacuum-dried overnight at 70°C.

110 To create the final composite, 0.5 g  $ZrCl_4$  and 1.5 g NH<sub>2</sub>-DFNS were combined with 10 mL of  
111 DMF in a vial, heated to 80°C (refer to Figure 1). In a separate vial, 0.7 g of terephthalic acid was  
112 dissolved in 10 mL of DMF at the same temperature. The prepared solutions were mixed and  
113 subjected to ultrasonic vibration for 30 minutes. The resulting mixture was then placed in a  
114 stainless-steel Teflon-lined autoclave and maintained at 120°C for 24 hours. Following this, the  
115 autoclave was cooled to room temperature, and the produced UiO-66@NH<sub>2</sub>-DFNS nanoparticles  
116 were filtered, washed multiple times with DMF and  $CHCl_3$ , and finally dried at 80°C using a  
117 vacuum oven.



118

119

**Figure 1.** Synthesis of UiO-66@NH<sub>2</sub>-DFNS

### 120 2.3. Characterisation of the materials

121 The surface characteristics and morphology of the synthesized UiO-66@NH<sub>2</sub>-DFNS were  
 122 examined using various analytical techniques. These included a scanning electron microscope  
 123 equipped with energy dispersive X-ray analysis (SEM-EDX, TECSAN VEGA3 model from Czech  
 124 Republic), a high-resolution transmission electron microscope (TEM, ZEISS LIBRA 200 FE from  
 125 Germany), N<sub>2</sub> adsorption at 77 K (BELSORP MINI from Osaka, Japan), X-ray diffraction (XRD,  
 126 Bruker AXS-D8 Advance from the USA) with Cu K $\alpha$  radiation, X-ray photoelectron spectroscopy  
 127 (XPS, Thermo Scientific Nexsa G2 from USA), and thermo-gravimetric analysis (TGA, Q600  
 128 from TA Instrument, the USA).

129 The collected N<sub>2</sub> adsorption/desorption data were analyzed using the Brunauer–Emmett–Teller  
 130 (BET) model, and the resulting BET surface area was reported for P/P<sub>0</sub> = 0.050 – 0.982 (BELSORP  
 131 MINI, Osaka, Japan). Additionally, the functional groups' type and quality were identified using  
 132 Fourier-transform infrared spectroscopy (FTIR, Perkin Elmer Spectrum 65 from the USA) in the  
 133 wave number range of 4000 to 400 cm<sup>-1</sup>. To determine the concentrations of DOX and TTC, a  
 134 UV-Vis spectrophotometer (AnalyticJena Specord 210 from Germany) and an HPLC system  
 135 (Agilent 1200 from the USA) were employed.

## 136 2.4. Photodegradation experiments

137 For initial investigations into adsorption-photodegradation, a uniform dispersion of 20 mg of UiO-  
138 66@NH<sub>2</sub>-DFNS nanocomposite was created in vials containing 10 mL of 100 mg.L<sup>-1</sup> DOX and  
139 TTC. The mixture was stirred in darkness for 0 to 10 minutes to establish an adsorption-desorption  
140 equilibrium. Subsequently, the suspension within the reactor was subjected to UV lamp radiation  
141 for varying durations (0 to 20 minutes) to study the photodegradation characteristics of the  
142 prepared samples. To eliminate UiO-66@NH<sub>2</sub>-DFNS nanoparticles, centrifugation was conducted  
143 at 9000 rpm for 10 minutes. The efficiency of degradation was determined by measuring the  
144 liquid's absorbance using a UV-Vis spectrophotometer at specific wavelengths: 275 nm for DOX  
145 and 357 nm for TTC. The remaining quantities of DOX and TTC in the samples were quantified  
146 through chromatographic analysis using an Agilent 1200 HPLC system.

## 147 2.5. Modeling and Optimisation Process

148 The chemometric approach involved utilizing a central composite design (CCD) within the  
149 framework of the response surface method (RSM), as outlined in reference <sup>52</sup>. Experimental data  
150 analysis was carried out using Design-Expert software (Trial Version 12, Stat-Ease, Inc.,  
151 Minneapolis, USA). The effects of three independent factors namely, sample pH, UiO-66@NH<sub>2</sub>-  
152 DFNS dose (mg.mL<sup>-1</sup>), and irradiation time on the photodegradation process were meticulously  
153 examined using the CCD. The degradation of DOX and TTC was identified as the desired  
154 outcomes for the proposed models. The three chosen variables (designated as A, B, and C) were  
155 converted into coded values at levels of -1.68, -1, 0, +1, and +1.68, as documented in Table 1.

156 **Table 1.** The experimental parameters and their levels for the CCD matrix.

Parameters	Levels				
	- $\alpha$	-1	0	+1	+ $\alpha$
A: Sample pH	2.0	3.0	4.5	6.0	7.0
B: UiO-66@NH <sub>2</sub> -DFNS dose (mg.mL <sup>-1</sup> )	0.32	1.0	2.0	3.0	3.68
C: Radiation time (min)	3.2	10	15	20	36.8

157

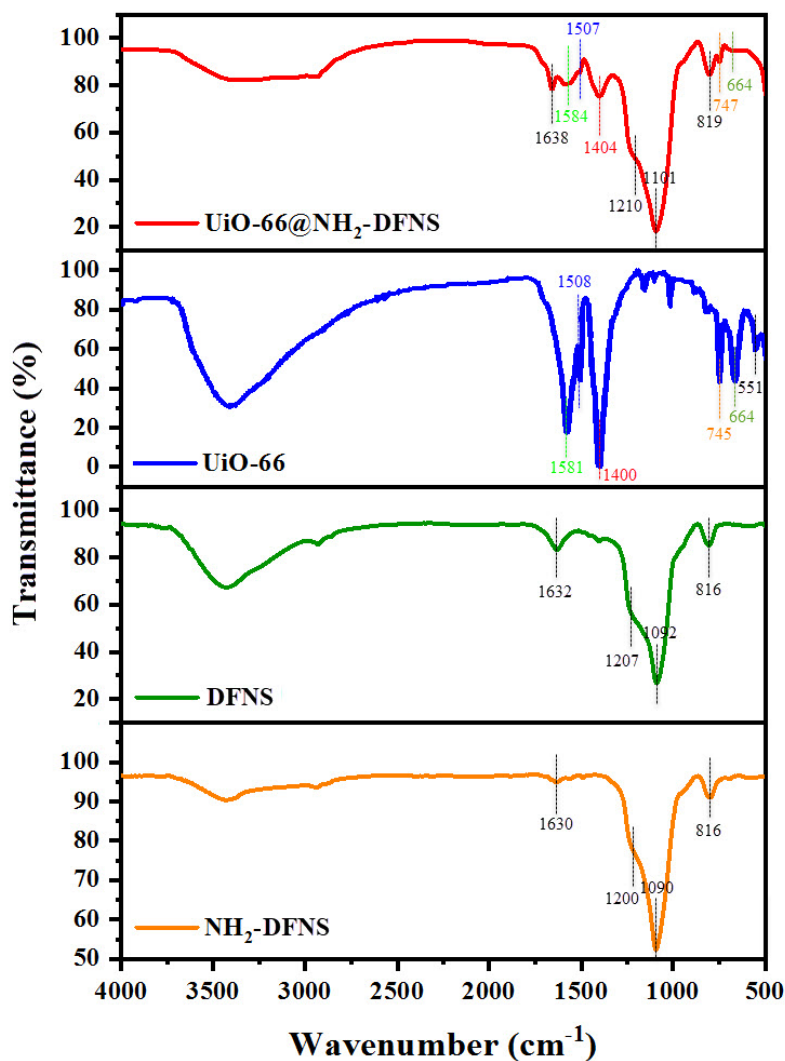
### 158 3. Results and discussion

159 After synthesising DFNS, UiO-66, and UiO-66@NH<sub>2</sub>-DFNS, the prepared materials' properties  
160 and photocatalytic performance were assessed and compared with the literature, as described in  
161 the following sections. Before the use of synthesised substrates, synthesised catalysts were  
162 identified using FTIR, XRD, DRS, BET, TGA, SEM-EDX, TEM, and XPS. Also, its zeta potential  
163 charge was determined to illustrate how UiO-66@NH<sub>2</sub>-DFNS nanocomposite interacts with  
164 negatively charged species.

#### 165 3.1. Characterisation

166 FTIR analysis serves as an effective method for examining surface functional groups in materials.  
167 In this study, transparent tablets were prepared using KBr to investigate FTIR spectra and identify  
168 the functional groups present in the synthesized materials, including DFNS, NH<sub>2</sub>-DFNS, UiO-66,  
169 and UiO-66@NH<sub>2</sub>-DFNS. The FTIR spectra for these synthesized substances are presented in  
170 Figure 2. For DFNS and NH<sub>2</sub>-DFNS, the spectral bands within the range of 3440–3220 cm<sup>-1</sup>  
171 corresponded to the O–H stretching band, while the O–H bending vibration manifested at 1632  
172 cm<sup>-1</sup> and 1630 cm<sup>-1</sup>, respectively. Bands around 1090–1200 cm<sup>-1</sup> indicated the asymmetric  
173 stretching of Si–O–Si, with a peak at 816 cm<sup>-1</sup> signifying symmetric vibrations of Si–O–Si in both  
174 DFNS and NH<sub>2</sub>-DFNS.

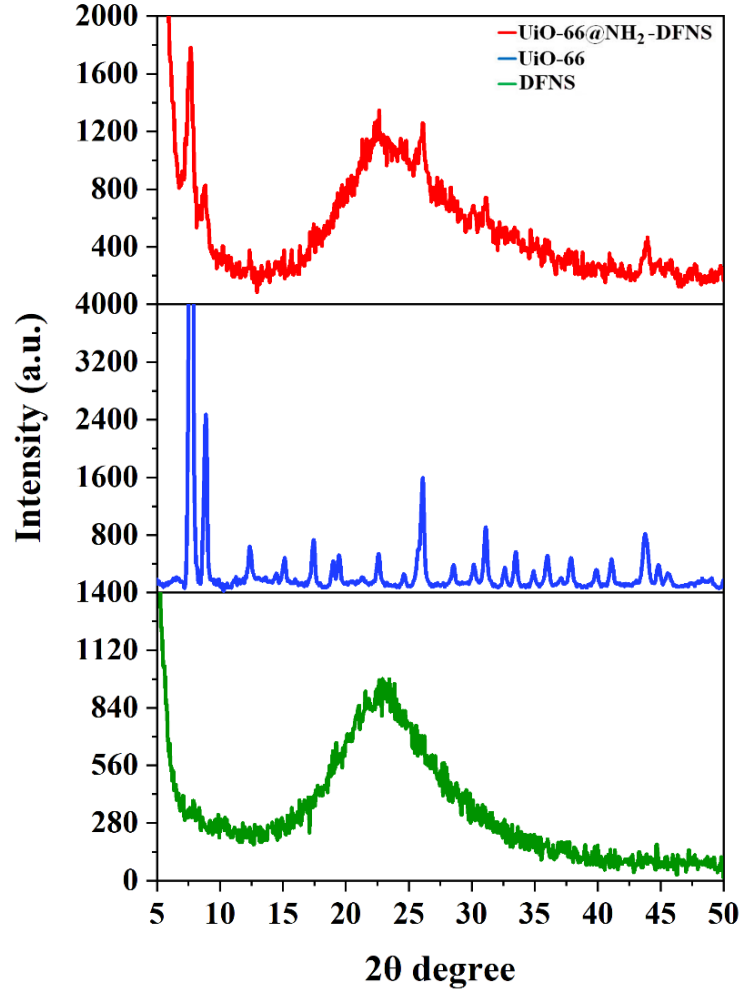
175 Within the FTIR spectra of UiO-66@NH<sub>2</sub>-DFNS, these bands were observed at 1638 cm<sup>-1</sup>, 1210  
176 cm<sup>-1</sup>, 1101 cm<sup>-1</sup>, and 819 cm<sup>-1</sup>, indicating the presence of DFNS within the nanocomposite.  
177 Moreover, absorption bands around 1580 cm<sup>-1</sup> and 1400 cm<sup>-1</sup> were attributed to the asymmetric  
178 and symmetric stretching vibration of carboxylate groups in the terephthalic ligands within the  
179 UiO-66 structure.<sup>29</sup> Notably, a weak band related to the C=C vibration of the benzene ring  
180 appeared at approximately 1507 cm<sup>-1</sup> for both UiO-66 and UiO-66@NH<sub>2</sub>-DFNS.<sup>29</sup> Additionally,  
181 a band at around 745 cm<sup>-1</sup> was linked to C-H vibrations of the ligands within the UiO-66 structure.  
182 The stretching vibration band at 664 cm<sup>-1</sup>, present in both UiO-66 and UiO-66@NH<sub>2</sub>-DFNS, was  
183 attributed to Zr-O within the MOF structure.<sup>29</sup> These findings collectively confirm the stable  
184 integration of UiO-66 onto the NH<sub>2</sub>-DFNS surface.



186 **Figure 2.** FTIR spectra of the synthesised DFNS, NH<sub>2</sub>-DFNS, UiO-66, and UiO-66@NH<sub>2</sub>-DFNS.

185  
 187 Figure 3 displays the arrangement of XRD at the  $2\theta$  scope of  $5\text{--}80^\circ$  for DFNS, and UiO-66@NH<sub>2</sub>-  
 188 DFNS. The wide peak observed between  $2\theta = 15\text{--}30^\circ$  for both DFNS and UiO-66@NH<sub>2</sub>-DFNS  
 189 samples indicates the presence of amorphous silica.<sup>53</sup> Furthermore, the emergence of new peaks  
 190 at  $2\theta = 7.7, 8.8, 12.3, 22.6, 26.1, 31.2, 44.0,$  and  $51.1^\circ$  in the XRD pattern of UiO-66@NH<sub>2</sub>-DFNS  
 191 corresponds to those found in other literature reports on UiO-66-based heterojunction  
 192 photocatalysts.<sup>29,38</sup> This alignment underscores the successful immobilization of UiO-66 onto the  
 193 surface of NH<sub>2</sub>-DFNS.





194

195

**Figure 3.** XRD pattern for the synthesised DFNS, UiO-66, and UiO-66@NH<sub>2</sub>-DFNS.

196

The UV–Vis diffuse reflectance spectroscopy (DRS) of UiO-66@NH<sub>2</sub>-DFNS nanocatalyst was performed to specify the band gap energy ( $E_g$ ). Light containing energy  $h\nu$  can pass through, reflect, or be absorbed by a material, depending on the magnitude of the energy. If the energy of the incident photons is lower than the energy of the band gap, the light will pass through the material, but if the energy of the band gap is higher, the light will be absorbed.  $E_g$  can be calculated using the absorption coefficient,  $\alpha$ , in the Tauc equation (Eq. 1).<sup>54</sup>

202

$$\alpha h\nu = A(h\nu - E_g)^m \quad (1)$$

203

where  $\alpha$  is the absorption coefficient,  $A$  is a constant,  $h\nu$  is photon energy, and  $E_g$  is band gap energy.  $m = 0.5$  is considered direct, and  $m = 2.0$  (Eq. 2) is an indirect transition type.

205

$$h\nu = (\alpha h\nu)^2 \quad (2)$$

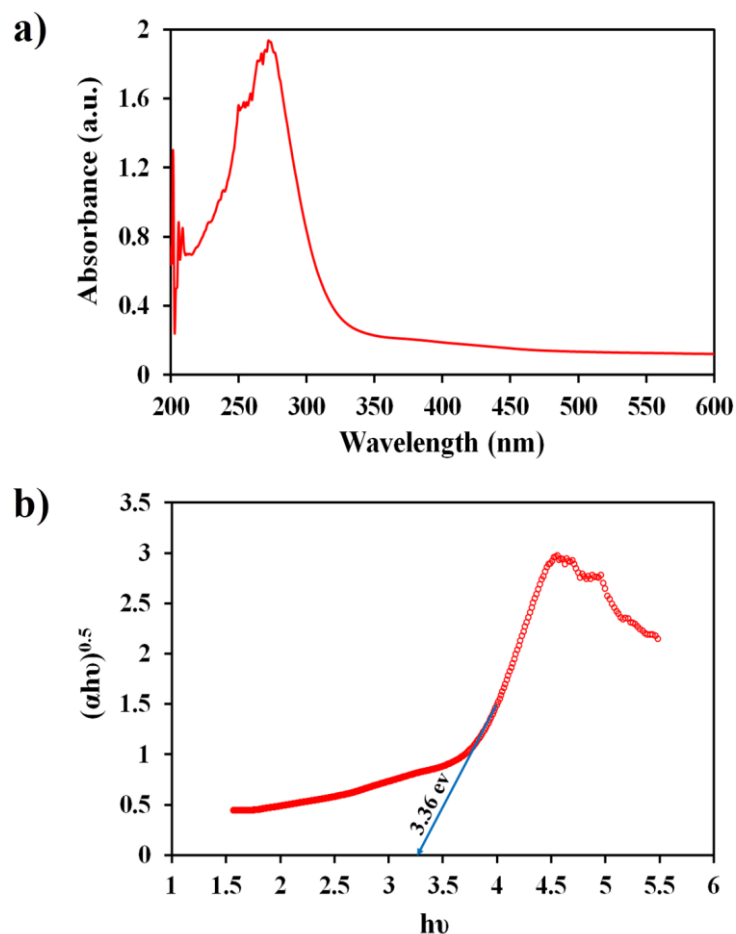
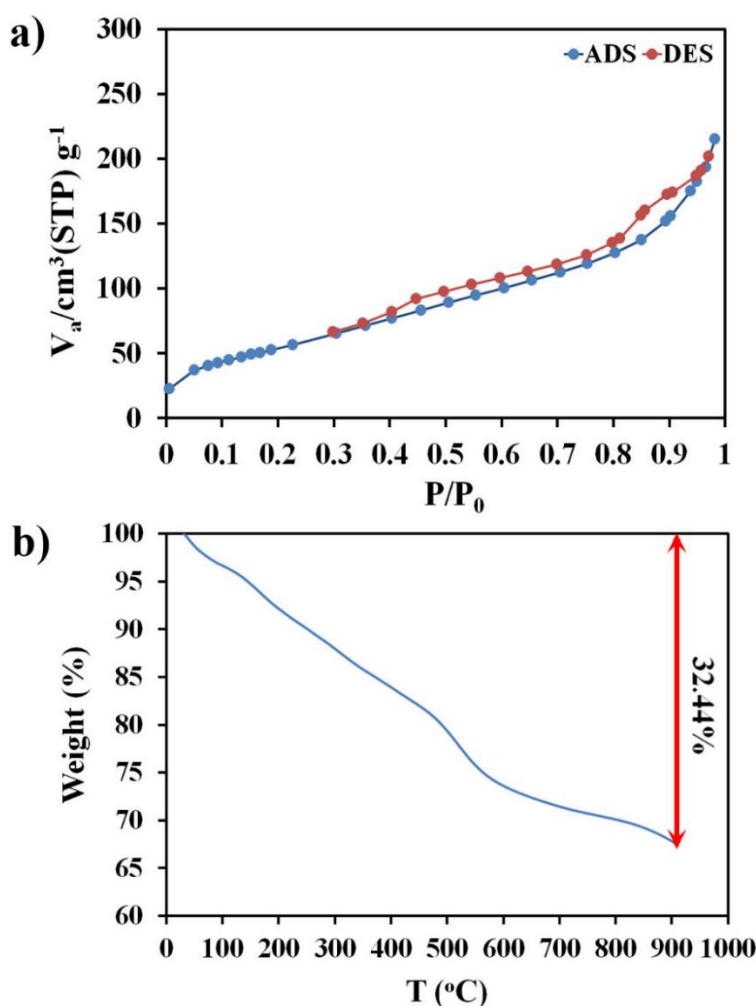


**Figure 4.** (a) UV-Vis, and (b) DRS for UiO-66@NH<sub>2</sub>-DFNS.

206  
 207  
 208 The band gap energy can be calculated by extrapolating the linear section of the  $(\alpha h\nu)^m$  with a  
 209 horizontal axis  $h\nu$  plot (Figure 4), as  $E_g = 3.36$  eV.<sup>55</sup> Even though DFNS and UiO-66 alone have  
 210 relatively wide band-gap energies, i.e. 4.04 and 3.60 eV, respectively,<sup>24,29,55,56</sup> the proposed UiO-  
 211 66@NH<sub>2</sub>-DFNS appears to have a narrower band-gap; thus can utilise effective photodegradation  
 212 response under lower energy radiation.<sup>24,29,55,56</sup>

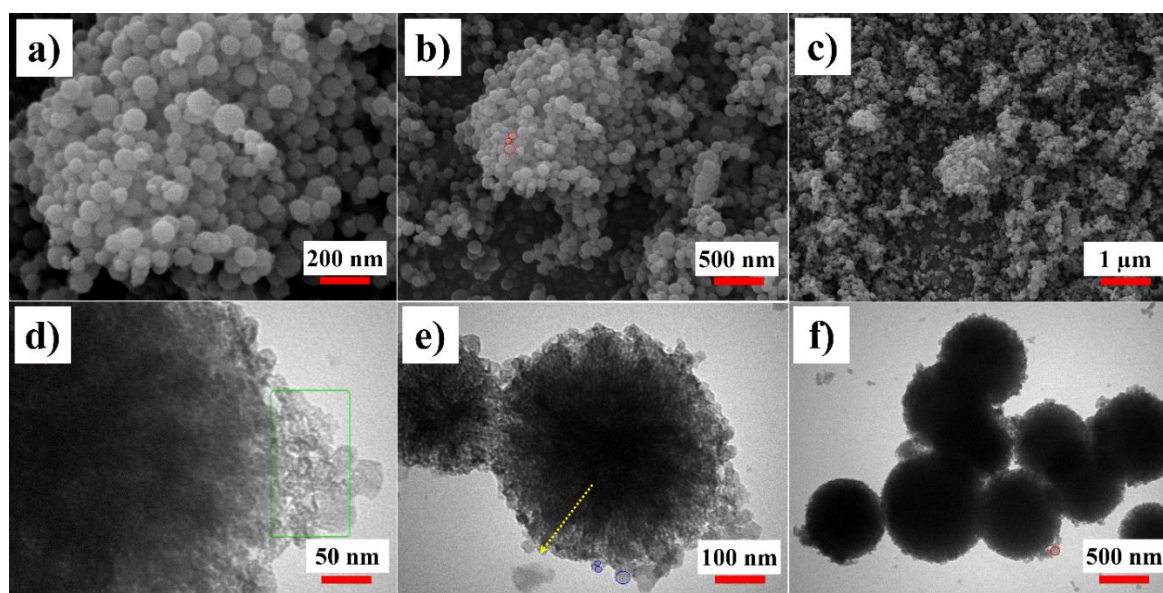
213 Specific surface area and pore dimensions of UiO-66@NH<sub>2</sub>-DFNS were specified by employing  
 214 nitrogen adsorption/desorption isotherm (Figure 5a). The UiO-66@NH<sub>2</sub>-DFNS exhibit type IV  
 215 isotherms, indicating a typical mesoporous structure, with unlimited monolayer-multilayer  
 216 adsorption for nitrogen adsorption at 77 K (Figure 5a).<sup>47,57-59</sup> In the first step, at low relative  
 217 pressures, the adsorption volume increases due to the interaction of the nitrogen molecules with  
 218 the more energetic section.<sup>58</sup> The showed rise in relative pressure, at  $P/P_0 = 0.45$ , relates to  
 219 multilayer formation when the monolayer formation of the adsorbed molecules is complete.<sup>57,60-63</sup>

220 Another rise in relative pressure, at  $P/P_0 = 0.85$ , indicates the bulk condensation of adsorbate  
 221 nitrogen gas.<sup>57,60-63</sup> This indicates capillary nitrogen condensation within uniform mesopores. A  
 222 significant shift in the adsorption branches toward lower relative pressures was also observed.  
 223 Hysteresis usually occurs when evaporation occurs from mesopores, thus causing desorption to  
 224 occur in a lower-pressure region than capillary condensation. As it is clear from Figure 5a, The H3  
 225 hysteresis loop of the UiO-66@NH<sub>2</sub>-DFNS has a similar mesoporous structure as DFNS. At  $P/P_0=$   
 226 0.982, the total pore volume was 0.3325 cm<sup>3</sup>.g<sup>-1</sup>. Based on t-plot calculations, the volume of  
 227 micropores was 0.1207 cm<sup>3</sup>.g<sup>-1</sup>, so a total of 36.3% of porosity can be attributed to micropores.<sup>47</sup>  
 228 Finally, the BET surface area of about 199.3 m<sup>2</sup>.g<sup>-1</sup> demonstrates that the UiO-66@NH<sub>2</sub>-DFNS  
 229 could be a suitable substrate for the catalyst.<sup>47,58</sup>



230  
 231 **Figure 5.** (a) Nitrogen adsorption-desorption isotherm at 77 K, and (b) TGA plot for UiO-66@NH<sub>2</sub>-DFNS.

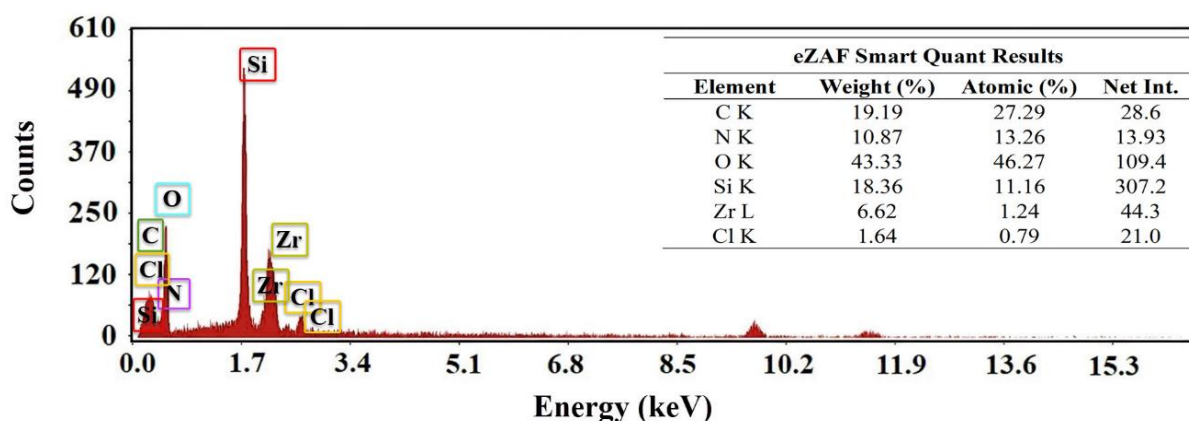
232 The thermal stability of UiO-66@NH<sub>2</sub>-DFNS was determined by TGA analysis under a nitrogen  
233 atmosphere with a heating rate of 10°C.min<sup>-1</sup> in the temperature range of 30–900 °C (Figure 5b).  
234 The TGA of UiO-66@NH<sub>2</sub>-DFNS shows three stages of weight loss about 32% . Before 100°C,  
235 a partial mass change of 7% was observed in the TGA curve of the UiO-66@NH<sub>2</sub>-DFNS  
236 nanocatalyst, which indicates the presence of physically adsorbed water molecules. The second  
237 mass loss of less than 5% at 150-200°C is attributed to the decomposition of DMF.<sup>64</sup> The third  
238 rapid mass loss at about 530-570°C is attributed to the decomposition of Zr-ligands in UiO-66  
239 structure to ZrO<sub>2</sub>.<sup>64</sup> Therefore, the prepared UiO-66@NH<sub>2</sub>-DFNS nanocatalyst is thermally stable  
240 at below 570 °C.



241  
242 **Figure 6.** SEM (a, b, and c), and TEM (d, e, and f) images for the synthesised UiO-66@NH<sub>2</sub>-DFNS.

243 The exterior surface morphology and elemental examination of UiO-66@NH<sub>2</sub>-DFNS were  
244 determined by TEM, SEM, and EDX analyses (Figs. 6 and 7). The morphology of UiO-66@NH<sub>2</sub>-  
245 DFNS is typical of DFNS-corresponding spherical nanoparticles with a homogeneous particle size  
246 distribution (some were illustrated as red circles in Figure 6b).<sup>65</sup> Figure 6 (d and e) obviously  
247 indicate the mounted UiO-66 crystalline shells on spherical DFNS nanoparticles.<sup>66</sup> Hollow-nature  
248 of the spherical DFNS nanoparticles is revealed by the contrast between the dark centre and the  
249 pale edge in the nanospheres (some shown as blue circles in Figure 6e).<sup>65</sup> Figure 6d, a higher  
250 magnification image demonstrates that the UiO-66 shells are porous structures with estimated pore  
251 sizes of below 10 nm. UiO-66 nanocrystals aggregation is also portrayed as a green rectangle.<sup>66</sup>

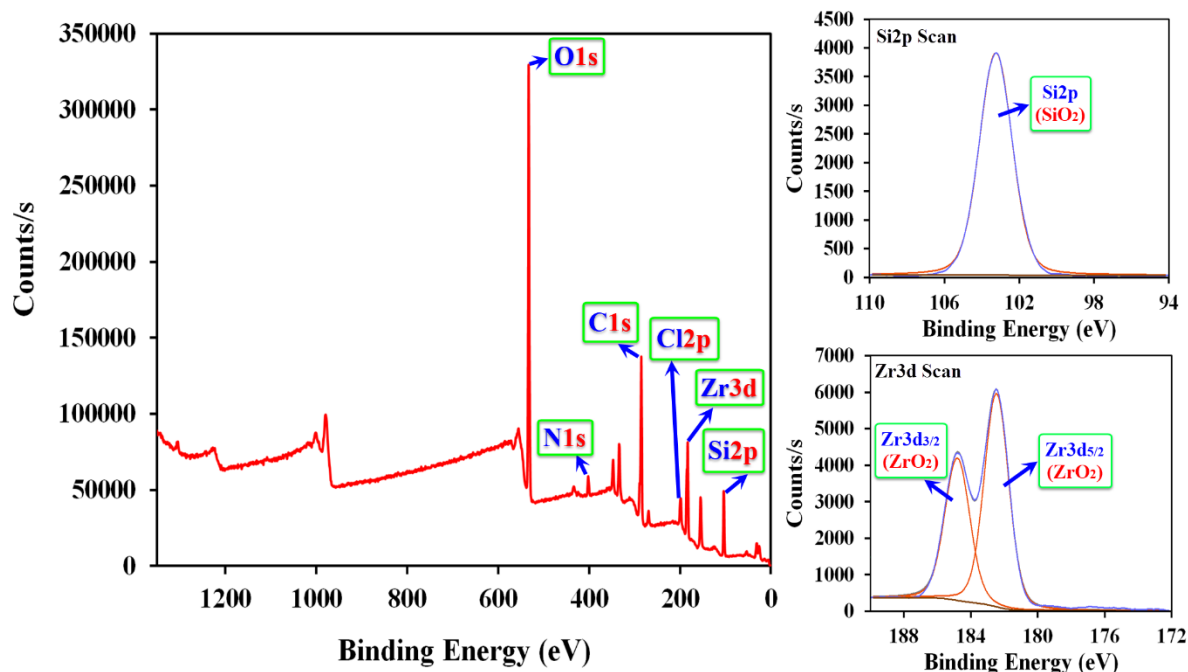
252 The UiO-66 nanocrystals grew inside and outside the pores of DFNS, forming a layer on the DFNS  
 253 surface in which the growth path was demonstrated as a yellow dashed arrow.<sup>67</sup> On the surface of  
 254 DFNS, the UiO-66 nanocrystals did not grow further due to the high concentration of Zr-ligands  
 255 used, but it sounds like the UiO-66 nanocrystals gradually fill the gaps between the crystals.<sup>67</sup> The  
 256 thickness of the UiO-66 layer increased as the gaps in the UiO-66@NH<sub>2</sub>-DFNS spheres were  
 257 continuously filled with UiO-66 nanocrystals, resulting in core-shell spheres in the UiO-66@NH<sub>2</sub>-  
 258 DFNS which is obvious in TEM images (see Figs. 6d and 6e). Also, the presence of Zr on UiO-  
 259 66@NH<sub>2</sub>-DFNS indicates the successful modification of DFNS with UiO-66 (Figure 7). All these  
 260 results showed the chemical bonding of UiO-66 on the NH<sub>2</sub>@DFNS outer layer and the production  
 261 of a nanocatalyst with regular uniform size (average size = 103 nm).



262

263

**Figure 7:** SEM-EDX analysis of proposed UiO-66@NH<sub>2</sub>-DFNS nanocomposite.



264  
 265 **Figure 8.** XPS analysis (XPS survey, Zr3d scan, and Si2p scan) for the synthesised UiO-66@NH<sub>2</sub>-DFNS  
 266 nanocatalyst.

267 The elemental composition of the prepared Ui-O66@NH<sub>2</sub>-DFNS nanocatalyst was analysed by  
 268 XPS, and the results are presented in Figure 8. The scanning spectrum confirmed the presence of  
 269 Si, Zr, Cl, C, N and O in the Si<sub>2p</sub>, Zr<sub>3d</sub>, Cl<sub>2p</sub>, C<sub>1s</sub>, N<sub>1s</sub>, and O<sub>1s</sub> binding energy zones of the fabricated  
 270 Ui-O66@NH<sub>2</sub>-DFNS. Si<sub>2p</sub> and Zr<sub>3d</sub> revealed peaks at 103.32 and 182.57 eV for O–Si–C and O–  
 271 Zr–C bonds, respectively.<sup>68</sup> The C–C, C=O, and C=N–C bonds were revealed at 284.67 eV and  
 272 the Cl<sub>2p</sub> peak at 198.18 eV corresponded to metal–Cl.<sup>69,70</sup> The peak corresponding to N<sub>1s</sub> appeared  
 273 at 401.52 for N–H in UiO-66@NH<sub>2</sub>-DFNS structure.<sup>68</sup> The O<sub>1s</sub> peak is shown to be 532.46 for Zr–  
 274 O and Si–O–C.<sup>68,71</sup> Also, the high-resolution XPS data in the zone of the Zr<sub>3d</sub> showed two peaks,  
 275 paralleling the 3d<sub>3/2</sub> and 3d<sub>5/2</sub> ZrO<sub>x</sub>.

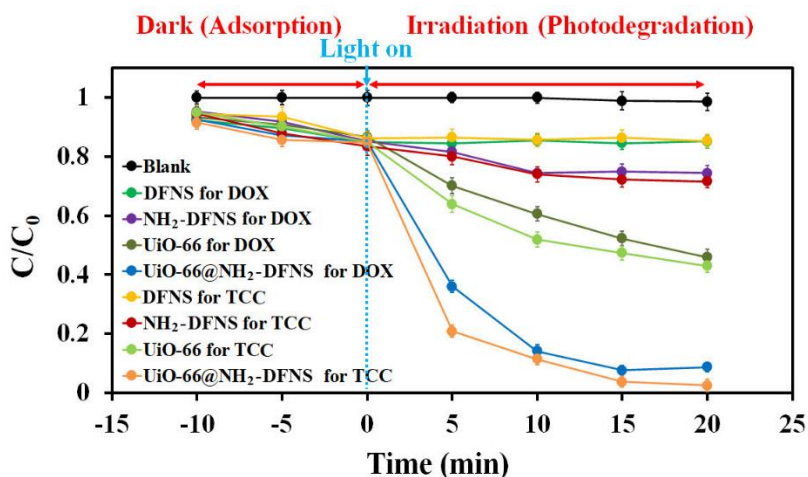
276 Finally, the zeta potential charge and mobility of UiO-66@NH<sub>2</sub>-DFNS were also analysed and  
 277 found to be 7.68 mV and 0.6017 μm.cm/Vs, respectively. It indicates a tendency of UiO-66@NH<sub>2</sub>-  
 278 DFNS nanocomposite to interact with negatively charged species.<sup>72</sup>

### 279 3.2. Photocatalytic Activity

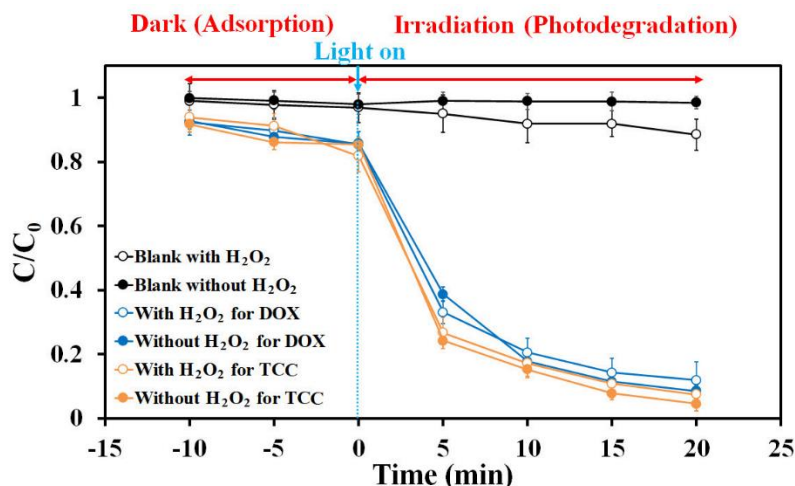
280 The preliminary investigations on the adsorption and photodegradation characteristics of the  
 281 nanocomposites were conducted based on the procedure described in Section 2.4. Based on the

282 results demonstrated in Figure 9, less than 16 % of DOX and TTC were removed in the first 10  
 283 minutes in the dark condition, mainly due to surface adsorption and no photodegradation was  
 284 involved. Using 2.0 mg.mL<sup>-1</sup> of UiO-66@NH<sub>2</sub>-DFNS resulted in a photodegradation efficiency  
 285 above 90% after 20 min irradiation. This value was about 15% for DFNS, 25% for NH<sub>2</sub>-DFNS,  
 286 attributing to H-bonding adsorptive interactions, and 54-58% for UiO-66. Higher  
 287 photodegradation efficiency of UiO-66@NH<sub>2</sub>-DFNS and UiO-66 under UV light in comparison  
 288 with DFNS and NH<sub>2</sub>-DFNS confirms the presence of UiO-66 alone or its immobilised sample on  
 289 the NH<sub>2</sub>-DFNS surface had a significant impact on its photodegradation properties.

290 The effect of reactive oxygen was analysed by using H<sub>2</sub>O<sub>2</sub> as reactive oxygen species (ROS) and  
 291 the experiments were performed with and without H<sub>2</sub>O<sub>2</sub>. As illustrated in Figure 10, there is no  
 292 significant difference in DOX and TTC photodegradation of the experiments. As a result, there is  
 293 no need to add H<sub>2</sub>O<sub>2</sub> to the solution when using the proposed UiO-66@NH<sub>2</sub>-DFNS.



294  
 295 **Figure 9:** Effect of irradiation time on the DOX and TTC photodegradations using DFNS, NH<sub>2</sub>-DFNS,  
 296 UiO-66, and UiO-66@NH<sub>2</sub>-DFNS. Process condition: photocatalyst dose = 2.0 mg.mL<sup>-1</sup>, DOX and TTC  
 297 concentration = 100 mg.L<sup>-1</sup>.



298  
 299 **Figure 10:** Effect of H<sub>2</sub>O<sub>2</sub> on the DOX and TTC photodegradations using UiO-66@NH<sub>2</sub>-DFNS. Process  
 300 condition: photocatalyst dose = 2.0 mg.mL<sup>-1</sup>, DOX and TTC concentration=100 mg.L<sup>-1</sup>.

### 301 3.3. Modeling and Optimisation

302 The effect of different variables of the sample pH, nanocatalyst dose, and irradiation time on the  
 303 photodegradation of DOX and TTC using UiO-66@NH<sub>2</sub>-DFNS was investigated by employing a  
 304 CCD-based template. The developed model was assessed by employing analysis of variance  
 305 (ANOVA). Considering the restricted number of variables to be optimised, only CCD was applied  
 306 and the screening was skipped. The CCD tests were performed based on the software design matrix  
 307 for solutions containing 200 mg.L<sup>-1</sup> of DOX and TTC. The following coded quadratic polynomial  
 308 model for the average photodegradation of DOX and TTC was derived by ANOVA and CCD  
 309 methodes.

$$310 \text{ Degradation}(\%) = 94.9 - 12.4A + 18.7B + 12.5C + 3.3AB + 6.7AC - 0.05BC - 6.9A^2 -$$

$$311 10.6B^2 - 8.4C^2 - 5.7D^2 \quad (3)$$

312 Positive and negative effects of each variable on the avreage photodegradation response are well  
 313 defined at this equation with positive and negative signs.. For both tetracycline-class pollutants  
 314 under investigation, the effect of sample pH on photodegradation was negative. However,  
 315 nanocomposite dose and irradiation time positively influenced photodegradation. The ANOVA  
 316 results of average photodegradation (Table 2) were on the basis of F-values and the mean squares  
 317 employed to predict the influence of the model and each variable in comparison with residuals.  
 318 The F-value of 273.11 was statistically significant. A lake of fit F-value of 2.91 revealed the  
 319 reliability of the model, showing the omitted terms were non-significant.<sup>7</sup>

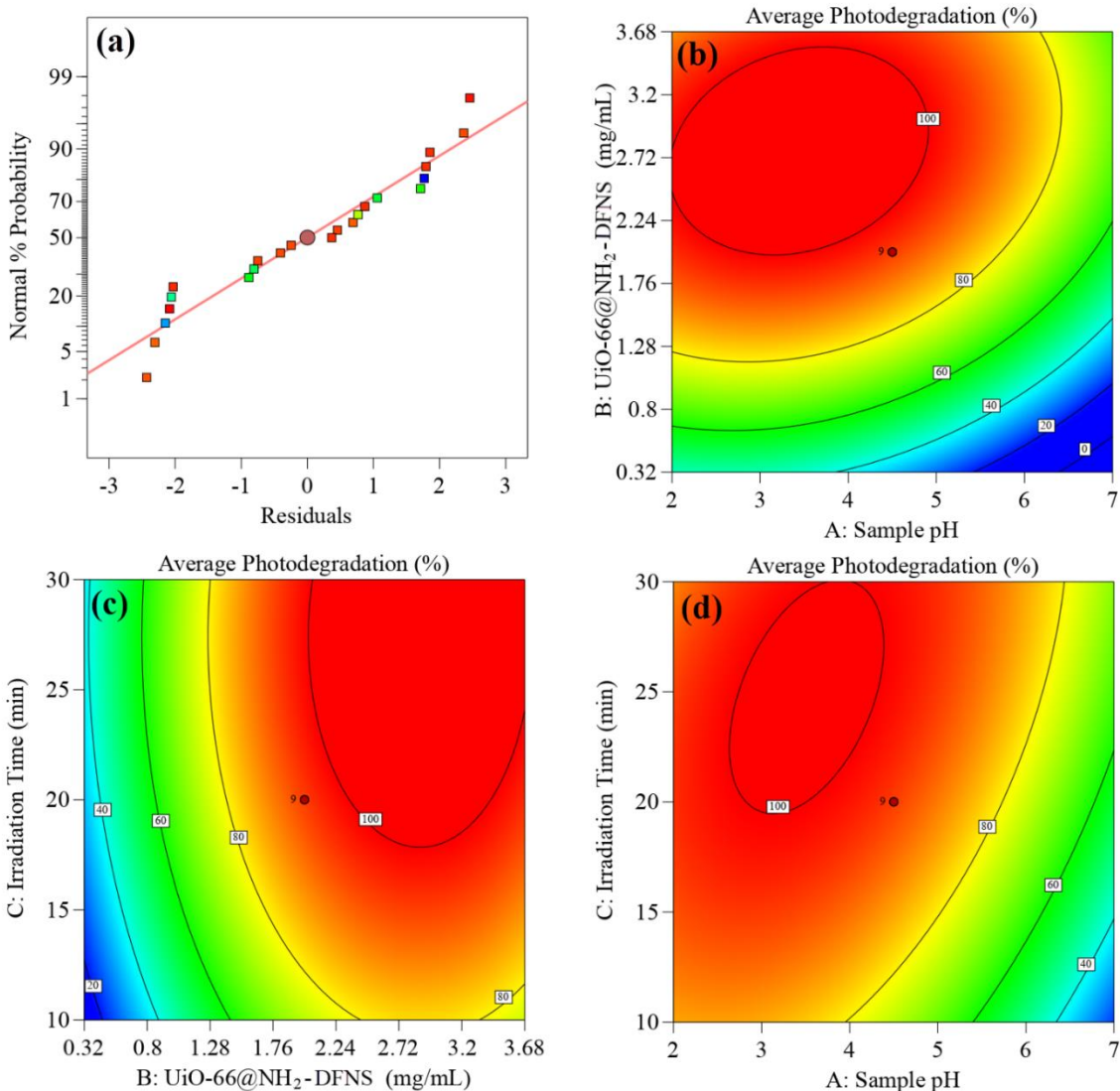


**Table 2.** The ANOVA for photodegradation efficiencies using UiO-66@NH<sub>2</sub>-DFNS.

Source	SS <sup>a</sup>	df <sup>b</sup>	MS <sup>c</sup>	F-value	p-value	
Model	13043.93	9	1449.33	273.11	< 0.0001	S <sup>e</sup>
A: Sample pH	2089.73	1	2089.73	393.78	< 0.0001	..
B: UiO-66@NH <sub>2</sub> -DFNS	4759.58	1	4759.58	896.88	< 0.0001	..
C: Irradiation time	2127	1	2127	400.8	< 0.0001	..
AB	87.12	1	87.12	16.42	0.0019	..
AC	359.12	1	359.12	67.67	< 0.0001	..
BC	0.02	1	0.02	0.0038	0.9521	NS <sup>f</sup>
A <sup>2</sup>	766.86	1	766.86	144.5	< 0.0001	S <sup>e</sup>
B <sup>2</sup>	1780.82	1	1780.82	335.57	< 0.0001	..
C <sup>2</sup>	1129.49	1	1129.49	212.84	< 0.0001	..
Residual	58.38	11	5.31			
LOF <sup>d</sup>	41.34	5	8.27	2.91	0.1128	NS <sup>f</sup>
Pure error	17.03	6	2.84			
Cor total	13135.71	22				

321 <sup>a</sup> Sum of squares; <sup>b</sup> Degree of freedom; <sup>c</sup> Mean square; <sup>d</sup> Lack of fit <sup>e</sup> significant; <sup>f</sup> not significant

322 The R<sup>2</sup> value of 0.9955 mirrored the concurrence between the experimental and estimated  
323 outcomes. In addition, the predicted R<sup>2</sup> of 0.9717 is in appropriate accordance with the adjusted  
324 R<sup>2</sup> of 0.9926, as it differed by around 2%. The normal probability of the residuals (Figure 11)  
325 revealed that residuals were randomly distributed around zero, indicating the model's reliability.<sup>7</sup>  
326 This acceptable normal distribution confirms the validity of the assumptions and independency  
327 behaviour in residuals.



328  
329 **Figure 11:** Normal probability (a) and response surface (b-d) plots for average photodegradation

330 The response surface graphs of the proposed model were employed to examine the interactions  
331 between the variables and portray their impact on photodegradation. As shown in Figure 11, pH-  
332 dose and pH-irradiation time affirmed strong interactions, as evidenced in the ANOVA Table  
333 (Table 2). In addition, a deeper attention at these graphs illustrated that decreasing the sample pH  
334 and increasing the UiO-66@NH<sub>2</sub>-DFNS dose and irradiation time increased the photodegradation  
335 efficiency. Meanwhile, the sample pHs lower than 5 showed acceptable photodegradation with  
336 moderate values of dose and time.

337 The photodegradation process was influenced positively by the dose of nanocomposite and  
338 irradiation duration. Notably, the UiO-66@NH<sub>2</sub>-DFNS dose had a more significant impact than

339 the irradiation time. On the other hand, the pH of the sample had a negative effect on the  
340 photodegradation efficiency, except for pH values below 5.0, which maintained consistent  
341 efficiency.

342 A change in pH value can affect the surface charge of UiO-66@NH<sub>2</sub>-DFNS, its photocatalytic  
343 capacity, and DOX/TTC ionisation state, so pH is a crucial factor in the degradation process.<sup>73,74</sup>  
344 At pH values lower than 5.0, hydrogen bonds between DOX/TTC and UiO-66@NH<sub>2</sub>-DFNS  
345 increased the catalytic decomposition rate, promoting the relocation of antibiotics from the  
346 solution to the UiO-66@NH<sub>2</sub>-DFNS outer layer. As shown in Figure 11b and 11d, the UiO-  
347 66@NH<sub>2</sub>-DFNS photocatalytic system demonstrated excellent efficiency even in acidic pHs,  
348 thanks to its interactions with negatively charged species based on zeta potential results,  
349 investigated in section 3.1.

350 The pH also influenced the ionisation state of DOX (pK<sub>a</sub> = 3.09)/TTC (pK<sub>a</sub> = 3.26), affecting the  
351 electrostatic forces between the molecules and the photocatalyst.<sup>73,74</sup> At pH below 3.0, DOX/TTC  
352 were mostly protonated, leading to strong electrostatic repulsion by the UiO-66@NH<sub>2</sub>-DFNS  
353 photocatalyst. At pH 3.0–5.0, the neutral forms (zwitterions) of DOX/TTC increased, resulting in  
354 better photocatalytic performance due to reduced electrostatic repulsion and enhanced hydrogen  
355 bonding forces. However, at pH over 5.0, the role of hydrogen bonding forces decreased, and the  
356 efficiency decreased significantly.

357 To confirm these findings, experiments were conducted at pH = 8.0, resulting in a significant  
358 decrease in photodegradation efficiency for solutions containing 200 mg.L<sup>-1</sup> of DOX and TTC  
359 (47.1 ± 8.5%). It is likely that at pHs above 7.0, anionic DOX/TTC molecules were attracted  
360 electrostatically by UiO-66@NH<sub>2</sub>-DFNS, but the hydrogen bonding forces, which were at their  
361 lowest level, played a more predominant role, leading to the observed decrease in efficiency.

362 A non-linear optimisation approach following the Nelder-Mead algorithm defined the optimum  
363 condition to achieve maximum photodegradation (95.7 ± 2.2%) for solutions containing 200 mg.L<sup>-1</sup>  
364 of DOX and TTC, pH= 4.2, nanocomposite quantity = 2.9 mg.mL<sup>-1</sup>, and irradiation time = 30  
365 min. The experimental tests at the optimised conditions achieved an average photodegradation of  
366 97.2±3.1, showing an excellent agreement between the experimental and CCD model's predicted  
367 data.

368 **3.4. Kinetic Investigations**

369 The rate of kinetic photodegradation of DOX and TTC under UV light were investigated within  
 370 the predetermined optimal conditions. By utilizing the identified best-case scenario, the data  
 371 obtained from the photodegradation process of DOX and TTC was fitted to the linearized  
 372 integrated forms of the zero-order (Eq. 4), pseudo-first-order (Eq. 5), and pseudo-second-order  
 373 (Eq. 6) kinetic models.<sup>75</sup>

374 
$$C_0 - C_t = k_{app}t \quad (4)$$

375 
$$\ln\left(\frac{C_0}{C_t}\right) = k_{app}t \quad (5)$$

376 
$$\frac{1}{C_t} - \frac{1}{C_0} = k_{app}t \quad (6)$$

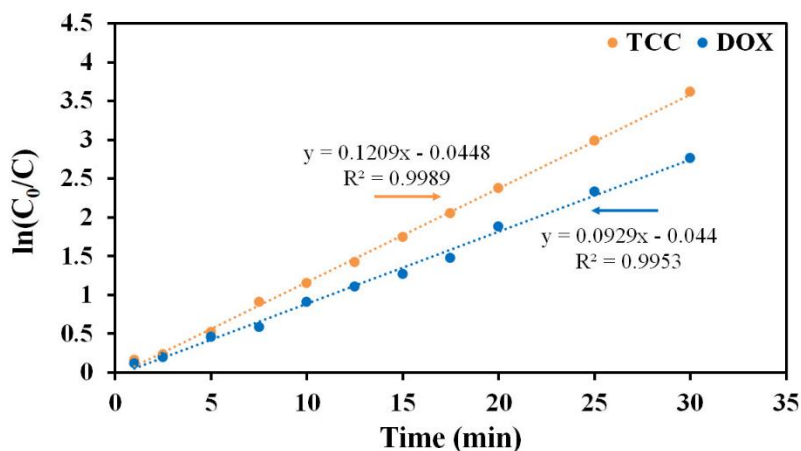
377 Where  $k_{app}$  is the apparent rate constant generated by  $k_{obs}$  and  $K_{an}$ ,  $k_{obs}$  is the rate constant,  $K_{an}$  is  
 378 the adsorption-desorption equilibrium constant and  $C_0$  and  $C_t$  ( $mg.L^{-1}$ ) are antibiotic concentration  
 379 at initial and time  $t$ .

380 Using Eq. 5, the linearised graphs for the photodegradation kinetics of DOX and TTC employing  
 381 UiO-66@NH<sub>2</sub>-DFNS nanocatalyst are portrayed in Figure 12. According to this figure, the  
 382 pseudo-first-order kinetic model with R<sup>2</sup> values of 0.9953 and 0.9989 for DOX and TTC fully  
 383 defined the photodegradation procedure. Moreover, the  $k_{app}$  values presented from the slope of the  
 384 graphs for DOX and TTC photodegradation are 0.0929 and 0.1209 min<sup>-1</sup>, respectively. The  $k_{app}$   
 385 values revealed a higher TTC photodegradation rate than the DOX degradation.

**Table 3:** Kinetic parameters for DOX and TTC photodegradation by UiO-66@NH<sub>2</sub>-DFNS. Process condition: sample pH = 4.2, photocatalyst dose = 2.9 mg.mL<sup>-1</sup>, DOX and TTC concentration = 200 mg.L<sup>-1</sup>.

Antibiotic	Zero-order		Pseudo-first order		Pseudo-second order	
	k <sub>0</sub> (min <sup>-1</sup> )	R <sup>2</sup>	k <sub>1</sub> (min <sup>-1</sup> )	R <sup>2</sup>	k <sub>2</sub> (min <sup>-1</sup> )	R <sup>2</sup>
DOX	5.8335	0.9018	0.0929	0.9953	0.0021	0.8371
TTC	5.7945	0.8378	0.1209	0.9989	0.0048	0.7672

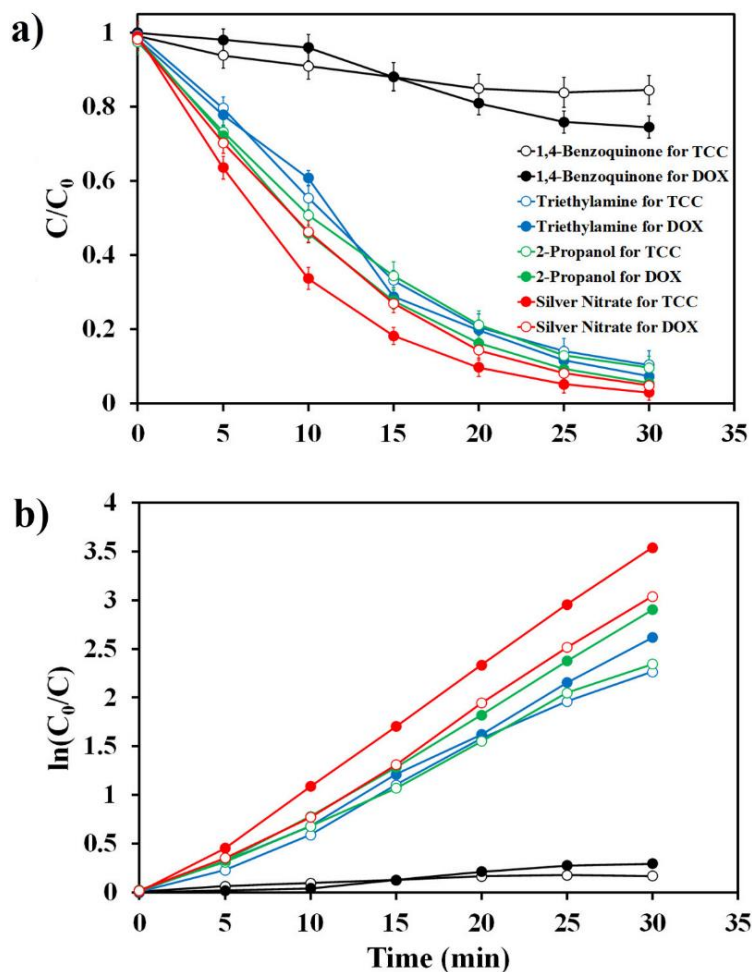
386



387  
 388 **Figure 12.** Kinetic fits of pseudo-first-order for DOX and TTC photodegradation by UiO-66@NH<sub>2</sub>-DFNS.  
 389 Process condition: sample pH = 4.2, photocatalyst dose = 2.9 mg.mL<sup>-1</sup>, DOX and TTC concentration = 200  
 390 mg.L<sup>-1</sup>.

### 391 3.5. Probable implemented mechanism

392 As shown in section 3.2 and Figure 9, the photodegradation of 100 mg.L<sup>-1</sup> solutions of DOX and  
 393 TTC in the presence of UiO-66@NH<sub>2</sub>-DFNS under UV irradiation can reach 95% in only 20  
 394 minutes. Superoxide (O<sub>2</sub><sup>•-</sup>) and hydroxyl (OH<sup>•</sup>) radicals, along with electrons (e<sup>-</sup>) and/or holes  
 395 (h<sup>+</sup>), can contribute to photo-assisted oxidation of DOX and TTC. The e<sup>-</sup> and h<sup>+</sup> are formed in a  
 396 semiconductor when the energy is greater than the band-gap, allowing a heterogeneous  
 397 photocatalysis reaction. The OH<sup>•</sup> can be produced by reacting surface adsorbed water ((H<sub>2</sub>O)<sub>ads</sub>)  
 398 with valence band holes (h<sub>VB</sub>). Also, the H<sub>2</sub>O<sub>2</sub> molecules can increase the concentration of the  
 399 produced OH<sup>•</sup> species. In addition, dissolved O<sub>2</sub> can interact with electrons in conduction bands  
 400 to produce O<sub>2</sub><sup>•-</sup>. To determine the role of these reactive species in photodegradation experiments,  
 401 various scavengers such as 1,4-benzoquinone, 2-propanol, silver nitrate, and tri-ethylamine were  
 402 used as reagents that investigated trapping for O<sub>2</sub><sup>•-</sup>, OH<sup>•</sup>, e<sup>-</sup>, and h<sup>+</sup>, respectively. As illustrated in  
 403 Figure 13, the 2-propanol, silver nitrate, and tri-ethylamine have no significant effect on the  
 404 photodegradation of DOX and TTC using the UiO-66@NH<sub>2</sub>-DFNS, suggesting a negligible  
 405 contribution from OH<sup>•</sup>, e<sup>-</sup>, and h<sup>+</sup>. In contrast, O<sub>2</sub><sup>•-</sup> radicals appear to be the most likely reactive  
 406 species involved in DOX and TTC photodegradation since 4-benzoquinone significantly  
 407 suppresses the activity of UiO-66@NH<sub>2</sub>-DFNS.<sup>29</sup> In agreement with these scavenger experiments,  
 408 Figure 10 demonstrates that H<sub>2</sub>O<sub>2</sub> has a negligible effect, which confirms that OH<sup>•</sup> is not involved  
 409 in the reaction.



410

411 **Figure 13** Effect of various scavengers on the DOX and TTC photodegradation using UiO-66@NH<sub>2</sub>-  
 412 DFNS. (a) C/C<sub>0</sub> vs time and (b) pseudo-first-order kinetic. Process condition: sample pH = 4.2,  
 413 photocatalyst dose = 2.9 mg.mL<sup>-1</sup>, DOX and TTC concentration = 200 mg.L<sup>-1</sup>.

### 414 3.6. Reusability Investigation

415 For long-term use, reusable photocatalysts are critical in saving energy and costs. Five repeat  
 416 degradation–washing–elution cycles under UV irradiation were conducted to verify the  
 417 photocatalyst's stability. After each cycle, the UiO-66@NH<sub>2</sub>-DFNS catalyst was centrifuged,  
 418 washed/eluted with DDW/EtOH, dried at 80°C, and reused. Mesoporous UiO-66@NH<sub>2</sub>-DFNS is  
 419 simultaneously regenerated into its initial form after washing/elution is completed. Based on the  
 420 results of the reusability investigation, photodegradation efficiencies stayed above 85% (Figure  
 421 14a). The photodegradation efficiencies decreased slightly, which can be attributed to the loss of  
 422 UiO-66@NH<sub>2</sub>-DFNS during several degradation-washing-elution cycles. The amount of

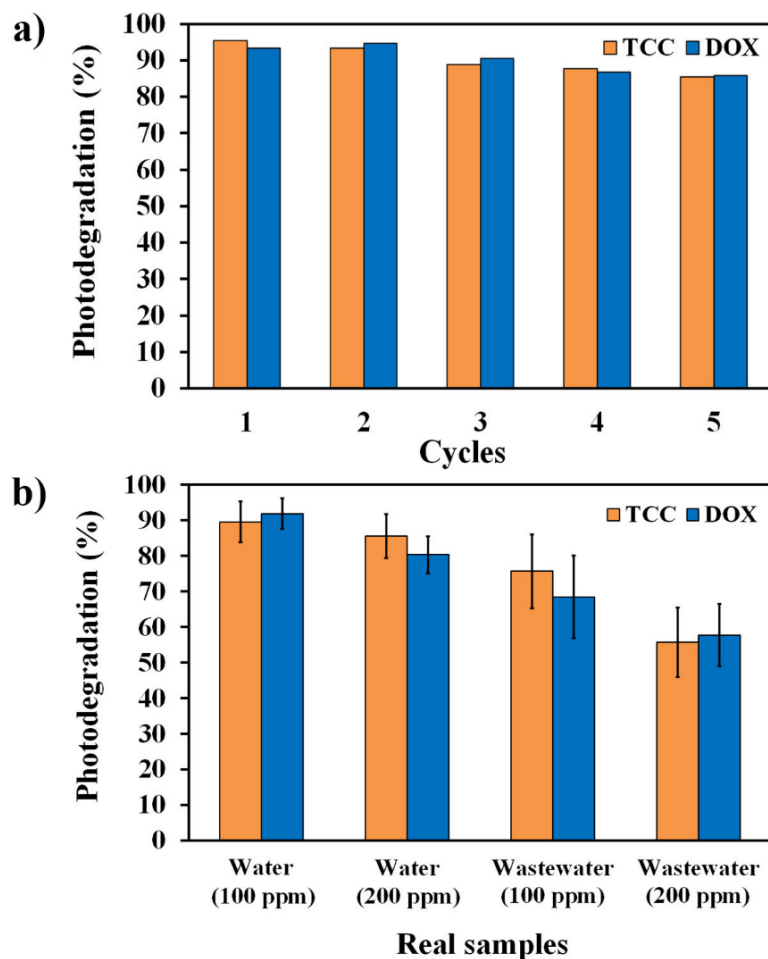
423 DOX/TTC eluted from the UiO-66@NH<sub>2</sub>-DFNS surface, however, was lower than the  
424 quantification limit, so they were not detected. This indicates adsorption of antibiotics has a  
425 negligible role in the proposed procedure, and we are faced with photodegradation as a  
426 predominant process.

427 This reusability study shows that the UiO-66@NH<sub>2</sub>-DFNS can be used for five cycles without  
428 significantly deteriorating its original photodegradation performance, which makes it an attractive  
429 candidate for water and wastewater treatment.

430

### 431 **3.7. Photodegradation Research on Actual Specimens**

432 Aiming to demonstrate the capability of the presented UiO-66@NH<sub>2</sub>-DFNS nanocatalyst for the  
433 degradation of DOX and TTC, tap water and effluent discharge of a pharmaceutical firm  
434 (Daropakhsh Pharmaceutical Chemical, Karaj, Tehran, Iran) were employed as actual specimens,  
435 and no DOX and TTC was discovered. The photodegradation capability outcomes of UiO-  
436 66@NH<sub>2</sub>-DFNS from actual samples which were spiked with 100 and 200 mg.L<sup>-1</sup> of DOX and  
437 TTC revealed the likely photodegradation results (Figure 14b). This specified that large amounts  
438 of several intervening species (e.g. cations such as Ca<sup>2+</sup>, Mg<sup>2+</sup>, Na<sup>+</sup>, K<sup>+</sup>, and so on, anions like  
439 HCO<sup>3-</sup>, Cl<sup>-</sup>, SO<sub>4</sub><sup>2-</sup>, PO<sub>4</sub><sup>3-</sup>, etc., and different pharmaceuticals and additives) in actual samples could  
440 not prevent the photodegradation process using UiO-66@NH<sub>2</sub>-DFNS. Hence, we are of the  
441 opinion that UiO-66@NH<sub>2</sub>-DFNS, as prepared, holds significant potential for use in the  
442 purification of water and wastewater.



443

444 **Figure 14:** (a) Reusability tests of UiO-66@NH<sub>2</sub>-DFNS, and (b) its performance in two real samples, i.e.  
 445 tap water and effluent of a pharmaceutical firm. Process condition: sample pH = 4.2, photocatalyst dose =  
 446 2.9 mg.mL<sup>-1</sup>, irradiation time = 30 min, DOX and TTC concentration = 100 and 200 mg.L<sup>-1</sup>.

### 447 3.8. Comparison with other reported nanocomposites

448 Several effective nanocomposites for removing DOX and TTC have been reported in the literature,  
 449 as shown in Table 4, in which their performance was compared with that of the synthesised UiO-  
 450 66@NH<sub>2</sub>-DFNS.<sup>7,76-80</sup> A significant advantage of UiO-66@NH<sub>2</sub>-DFNS over the reported  
 451 adsorbents is its photocatalytic property.<sup>78,79</sup> These reported substrates only bind antibiotics to their  
 452 surfaces through an adsorptive removal mechanism, which results into pollution transfer from  
 453 large aqueous media to the solid substrate with a small area. Based on the data shown in Table 4,  
 454 in comparison with catalytic and photocatalytic substrates, the proposed UiO-66@NH<sub>2</sub>-DFNS  
 455 accelerates the degradation of DOX and TTC by up to 200 mg.L<sup>-1</sup> in only 30 minutes at moderate



456 pH, which provides excellent photodegradation.<sup>7,76,77,80</sup> Besides, good kinetic constant and the easy  
 457 and fast synthesis together with up to five times reusability without a significant decrease in  
 458 photodegradation efficiency makes UiO-66@NH<sub>2</sub>-DFNS a unique nanocomposite.

459 **Table 4.** Comparison of UiO-66@NH<sub>2</sub>-DFNS with other reported nanocomposites in DOX and  
 460 TTC removal.

Nanocomposite	Removal mechanism	pH	Dose (mg.mL <sup>-1</sup> )	Conc. (mg.L <sup>-1</sup> )	Time (min )	Kinetic constant (min <sup>-1</sup> )	Ref.
Birnessite	Photocatalytic	8.0	0.67	50	30	NR <sup>a</sup>	76
Ce/Fe	Catalytic	7.0	2.0	10	60	0.0232	77
Graphene oxide@Fe-Cu-Ag	Catalytic	2.0	3.0	50	30	0.0457	7
Schwertmannite	Catalytic	2.0	1.6	20	120	0.0540- 0.1492	80
Graphene oxide/Mg-Zn-Al	Adsorptive	8.0	1.5	100	90	0.0021	78
syzygium cumini l. Wood biochar	Adsorptive	7.0	1.0	20	60	0.0300	79
UiO-66@NH <sub>2</sub> -DFNS	Photocatalytic	4.2	2.9	200	30	0.0929- 0.1209	This work

<sup>a</sup>Not reported.

461

#### 462 4. Conclusions

463 This study successfully developed and characterised an innovative UiO-66 nanocomposite  
 464 photocatalyst for the efficient photodegradation of tetracycline-class antibiotics, including  
 465 doxycycline and tetracycline. The immobilisation of UiO-66 on NH<sub>2</sub>-DFNS was confirmed  
 466 through characterisation analyses, resulting in an excellent heterojunction, a narrow band-gap  
 467 energy, and a large specific surface area, all contributing to enhanced photocatalytic performance.

468 Utilising a central composite design, various reaction variables were optimised, leading to the  
 469 photocatalyst achieving a remarkable degradation efficiency of  $97.2 \pm 3.1$  for aqueous media  
 470 containing 200 mg.L<sup>-1</sup> of doxycycline and tetracycline under defined optimal conditions: pH =  
 471 4.2, nanocomposite dose = 2.9 mg.mL<sup>-1</sup>, and irradiation time = 30 min. The experimental results  
 472 satisfy the model predictions ( $95.7 \pm 2.2\%$ ).

473 The oxidation of doxycycline and tetracycline was found to be the primary degradation process,  
474 facilitated by superoxide radical anions on the UiO-66@NH<sub>2</sub>-DFNS surface, derived from the  
475 oxidation of water and dissolved oxygen molecules. Kinetic showed that the experimental data  
476 followed a pseudo-first-order model, and indicated that the surface reaction was the rate-  
477 determining step.

478 Our experiments demonstrated that the proposed materials exhibited significantly superior  
479 degradation of tetracycline-class antibiotics compared to other methods. The advantages included  
480 rapid degradation in just 30 minutes, moderate pH conditions, an excellent kinetic constant, ease  
481 and speed of synthesis, and a five-fold increase in reusability without a significant decrease in  
482 photodegradation efficiency, resulting in excellent photodegradation performance using this  
483 unique nanocomposite.

#### 484 **Author contribution**

485 **Fatemeh Deymeh:** Conceptualization, Methodology, Investigation, Writing – original draft,  
486 Writing – review & editing, Visualisation. **Ali Ahmadpour:** Conceptualization, Review & editing,  
487 Supervision, Funding acquisition. **Ali Allahresani:** Conceptualization, Review & editing,  
488 Advisor, **Arash Arami-Niya:** Conceptualization, Review & editing, Advisor,

#### 489 **Declaration of Competing Interest**

490 The authors declare that they have no known competing financial interests or personal  
491 relationships that could have appeared to influence the work reported in this paper.

#### 492 **Acknowledgments**

493 The authors appreciate the support of the Ferdowsi University of Mashhad, Iran (Grant No. 54010)  
494 for this work.

#### 495 **References**

- 496 (1) Shahat, A.; Kubra, K. T.; Salman, M. S.; Hasan, M. N.; Hasan, M. M. Novel Solid-State  
497 Sensor Material for Efficient Cadmium(II) Detection and Capturing from Wastewater.  
498 *Microchem. J.* **2021**, *164*, 105967. <https://doi.org/10.1016/J.MICROC.2021.105967>.
- 499 (2) Awual, M. R. A Novel Facial Composite Adsorbent for Enhanced Copper(II) Detection  
500 and Removal from Wastewater. *Chem. Eng. J.* **2015**, *266*, 368–375.  
501 <https://doi.org/10.1016/j.cej.2014.12.094>.
- 502 (3) Hasan, M. N.; Shenashen, M. A.; Hasan, M. M.; Znad, H.; Awual, M. R. Assessing of

- 503 Cesium Removal from Wastewater Using Functionalized Wood Cellulosic Adsorbent.  
504 *Chemosphere* **2021**, 270, 128668. <https://doi.org/10.1016/j.chemosphere.2020.128668>.
- 505 (4) Hasan, M. M.; Salman, M. S.; Hasan, M. N.; Rehan, A. I.; Awual, M. E.; Rasee, A. I.;  
506 Waliullah, R. M.; Hossain, M. S.; Kubra, K. T.; Sheikh, M. C.; Khaleque, M. A.;  
507 Marwani, H. M.; Islam, A.; Awual, M. R. Facial Conjugate Adsorbent for Sustainable  
508 Pb(II) Ion Monitoring and Removal from Contaminated Water. *Colloids Surfaces A*  
509 *Physicochem. Eng. Asp.* **2023**, 673, 131794.  
510 <https://doi.org/10.1016/j.colsurfa.2023.131794>.
- 511 (5) Awual, M. R. Efficient Phosphate Removal from Water for Controlling Eutrophication  
512 Using Novel Composite Adsorbent. *J. Clean. Prod.* **2019**, 228, 1311–1319.  
513 <https://doi.org/10.1016/J.JCLEPRO.2019.04.325>.
- 514 (6) Awual, M. R.; Hasan, M. M.; Islam, A.; Rahman, M. M.; Asiri, A. M.; Khaleque, M. A.;  
515 Sheikh, M. C. Introducing an Amine Functionalized Novel Conjugate Material for Toxic  
516 Nitrite Detection and Adsorption from Wastewater. *J. Clean. Prod.* **2019**, 228, 778–785.  
517 <https://doi.org/10.1016/j.jclepro.2019.04.280>.
- 518 (7) Hemmat, K.; Khodabakhshi, M. R.; Zeraatkar Moghaddam, A. Synthesis of Nanoscale  
519 Zero-Valent Iron Modified Graphene Oxide Nanosheets and Its Application for Removing  
520 Tetracycline Antibiotic: Response Surface Methodology. *Appl. Organomet. Chem.* **2021**,  
521 35 (1), e6059. <https://doi.org/10.1002/AOC.6059>.
- 522 (8) Rehan, A. I.; Rasee, A. I.; Awual, M. E.; Waliullah, R. M.; Hossain, M. S.; Kubra, K. T.;  
523 Salman, M. S.; Hasan, M. M.; Hasan, M. N.; Sheikh, M. C.; Marwani, H. M.; Khaleque,  
524 M. A.; Islam, A.; Awual, M. R. Improving Toxic Dye Removal and Remediation Using  
525 Novel Nanocomposite Fibrous Adsorbent. *Colloids Surfaces A Physicochem. Eng. Asp.*  
526 **2023**, 673, 131859. <https://doi.org/10.1016/j.colsurfa.2023.131859>.
- 527 (9) Moghaddam, A. Z.; Jazi, M. E.; Allahrasani, A.; Ganjali, M. R.; Badiiei, A. Removal of  
528 Acid Dyes from Aqueous Solutions Using a New Eco-Friendly Nanocomposite of  
529 CoFe<sub>2</sub>O<sub>4</sub> Modified with Tragacanth Gum. *J. Appl. Polym. Sci.* **2020**, 137 (17), 48605.  
530 <https://doi.org/10.1002/APP.48605>.
- 531 (10) Yang, X.; Chen, Z.; Zhao, W.; Liu, C.; Qian, X.; Zhang, M.; Wei, G.; Khan, E.; Hau Ng,  
532 Y.; Sik Ok, Y. Recent Advances in Photodegradation of Antibiotic Residues in Water.  
533 *Chem. Eng. J.* **2021**, 405, 126806–126830. <https://doi.org/10.1016/j.cej.2020.126806>.
- 534 (11) Hoslett, J.; Ghazal, H.; Katsou, E.; Jouhara, H. The Removal of Tetracycline from Water  
535 Using Biochar Produced from Agricultural Discarded Material. *Sci. Total Environ.* **2021**,  
536 751, 141755–141765. <https://doi.org/10.1016/J.SCITOTENV.2020.141755>.
- 537 (12) Xing, Z. P.; Sun, D. Z. Treatment of Antibiotic Fermentation Wastewater by Combined  
538 Polyferric Sulfate Coagulation, Fenton and Sedimentation Process. *J. Hazard. Mater.*  
539 **2009**, 168 (2–3), 1264–1268. <https://doi.org/10.1016/j.jhazmat.2009.03.008>.
- 540 (13) Li, Q.; Ji, M.; Li, X.; Song, H.; Wang, G.; Qi, C.; Li, A. Efficient Co-Removal of Copper  
541 and Tetracycline from Aqueous Solution by Using Permanent Magnetic Cation Exchange  
542 Resin. *Bioresour. Technol.* **2019**, 293, 122068.  
543 <https://doi.org/10.1016/J.BIORTECH.2019.122068>.
- 544 (14) Alonso, J. J. S.; El Kori, N.; Melián-Martel, N.; Del Río-Gamero, B. Removal of

- 545 Ciprofloxacin from Seawater by Reverse Osmosis. *J. Environ. Manage.* **2018**, *217*, 337–  
546 345. <https://doi.org/10.1016/j.jenvman.2018.03.108>.
- 547 (15) Lan, L.; Kong, X.; Sun, H.; Li, C.; Liu, D. High Removal Efficiency of Antibiotic  
548 Resistance Genes in Swine Wastewater via Nanofiltration and Reverse Osmosis  
549 Processes. *J. Environ. Manage.* **2019**, *231*, 439–445.  
550 <https://doi.org/10.1016/j.jenvman.2018.10.073>.
- 551 (16) Wang, L.; Liu, Y.; Pang, D.; Song, H.; Zhang, S. Simultaneous Electrochemical  
552 Degradation of Tetracycline and Metronidazole through a High-Efficiency and Low-  
553 Energy-Consumption Advanced Oxidation Process. *Chemosphere* **2022**, *292*, 133469.  
554 <https://doi.org/10.1016/J.CHEMOSPHERE.2021.133469>.
- 555 (17) Gao, G.; Zhang, X.; Wang, P.; Ren, Y.; Meng, X.; Ding, Y.; Zhang, T.; Jiang, W.  
556 Electrochemical Degradation of Doxycycline Hydrochloride on Bi/Ce Co-Doped Ti/PbO<sub>2</sub>  
557 Anodes: Efficiency and Mechanism. *J. Environ. Chem. Eng.* **2022**, *10* (5), 108430.  
558 <https://doi.org/10.1016/J.JECE.2022.108430>.
- 559 (18) Yin, F.; Lin, S.; Zhou, X.; Dong, H.; Zhan, Y. Fate of Antibiotics during Membrane  
560 Separation Followed by Physical-Chemical Treatment Processes. *Sci. Total Environ.*  
561 **2021**, *759*, 143520–143528. <https://doi.org/10.1016/j.scitotenv.2020.143520>.
- 562 (19) Xu, Z.; Jia, Y.; Zhang, X.; Hu, S.; Luo, Y.; He, H.; Chen, B.; Huang, B.; Pan, X. Algal  
563 Organic Matter Accelerates the Photodegradation of Tetracycline: Mechanisms,  
564 Degradation Pathways and Product Toxicity. *Chem. Eng. J.* **2023**, *468*, 143724.  
565 <https://doi.org/10.1016/J.CEJ.2023.143724>.
- 566 (20) Li, J.; Song, Y.; Wei, Z.; Wang, F.; Zhang, X.; Zhu, H.; Sheng, S.; Zou, H. Unique  
567 Kinetics Feature and Excellent Photocatalytic Performance of Tetracycline  
568 Photodegradation Using Yolk-Shell TiO<sub>2</sub>@void@TiO<sub>2</sub>:Eu<sup>3+</sup>. *Appl. Catal. A Gen.* **2023**,  
569 *650*, 119008. <https://doi.org/10.1016/J.APCATA.2022.119008>.
- 570 (21) Huang, L.; Liu, H.; Wang, Y.; Zhang, T. C.; Yuan, S. Construction of Ternary  
571 Bi<sub>2</sub>O<sub>3</sub>/Biochar/g-C<sub>3</sub>N<sub>4</sub> Heterojunction to Accelerate Photoinduced Carrier Separation for  
572 Enhanced Tetracycline Photodegradation. *Appl. Surf. Sci.* **2023**, *616*, 156509.  
573 <https://doi.org/10.1016/J.APSUSC.2023.156509>.
- 574 (22) Sivaranjani, P. R.; Syed, A.; Elgorban, A. M.; Bahkali, A. H.; Balakrishnaraja, R.; Varma,  
575 R. S.; Sudheer Khan, S. Fabrication of Ternary Nano-Heterojunction via Hierarchical  
576 Deposition of  $\alpha$ -Fe<sub>2</sub>O<sub>3</sub> and  $\beta$ -La<sub>2</sub>S<sub>3</sub> on Cubic CoCr<sub>2</sub>O<sub>4</sub> for Enhanced Photodegradation  
577 of Doxycycline. *J. Ind. Eng. Chem.* **2023**, *118*, 407–417.  
578 <https://doi.org/10.1016/J.JIEC.2022.11.025>.
- 579 (23) Ding, R.; Ouyang, Z.; Zhang, X.; Dong, Y.; Guo, X.; Zhu, L. Biofilm-Colonized versus  
580 Virgin Black Microplastics to Accelerate the Photodegradation of Tetracycline in Aquatic  
581 Environments: Analysis of Underneath Mechanisms. *Environ. Sci. Technol.* **2023**, *57* (14),  
582 5714–5725.  
583 [https://doi.org/10.1021/ACS.EST.3C00019/SUPPL\\_FILE/ES3C00019\\_SI\\_001.PDF](https://doi.org/10.1021/ACS.EST.3C00019/SUPPL_FILE/ES3C00019_SI_001.PDF).
- 584 (24) Deymeh, F.; Ahmadpour, A.; Allahresani, A. Binary Antibiotics Degradation Employing  
585 an Efficient Direct Z-Scheme Ti(VI)-Salen Complex Loaded on Dendritic Fibrous Nano-  
586 Silica. *Water. Air. Soil Pollut.* **2023**, *234* (4), 1–24. <https://doi.org/10.1007/S11270-023->

- 587 06272-1/METRICS.
- 588 (25) Yang, L.; Yuan, C.; Chen, X.; Xue, W.; Cao, G.; Meng, S.; Bai, L. The Effect of  
589 Nitrification Inhibitors on the Aerobic Biodegradation of Tetracycline Antibiotics in  
590 Swine Wastewater. *Chemosphere* **2023**, *311*, 136849.  
591 <https://doi.org/10.1016/J.CHEMOSPHERE.2022.136849>.
- 592 (26) Liu, M.; Gao, Y.; Wang, Y.; Li, Y.; Zou, D. Status and Opportunities in the Treatment of  
593 Tetracyclines from Aquatic Environments by Metal-Organic Frameworks (MOFs) and  
594 MOFs-Based Composites. *Mater. Today Chem.* **2022**, *26*, 101209–101230.  
595 <https://doi.org/10.1016/J.MTCHEM.2022.101209>.
- 596 (27) Wu, S.; Hu, H.; Lin, Y.; Zhang, J.; Hu, Y. H. Visible Light Photocatalytic Degradation of  
597 Tetracycline over TiO<sub>2</sub>. *Chem. Eng. J.* **2020**, *382*, 122842–122852.  
598 <https://doi.org/10.1016/j.cej.2019.122842>.
- 599 (28) Wang, C. C.; Wang, X.; Liu, W. The Synthesis Strategies and Photocatalytic  
600 Performances of TiO<sub>2</sub>/MOFs Composites: A State-of-the-Art Review. *Chem. Eng. J.*  
601 **2020**, *391*, 123601. <https://doi.org/10.1016/j.cej.2019.123601>.
- 602 (29) Wang, Y. L.; Zhang, S.; Zhao, Y. F.; Bedia, J.; Rodriguez, J. J.; Bolver, C. UiO-66-Based  
603 Metal Organic Frameworks for the Photodegradation of Acetaminophen under Simulated  
604 Solar Irradiation. *J. Environ. Chem. Eng.* **2021**, *9* (5), 106087–110697.  
605 <https://doi.org/10.1016/j.jece.2021.106087>.
- 606 (30) Swetha, S.; Janani, B.; Khan, S. S. A Critical Review on the Development of Metal-  
607 Organic Frameworks for Boosting Photocatalysis in the Fields of Energy and  
608 Environment. *J. Clean. Prod.* **2022**, *333*, 130164–130182.  
609 <https://doi.org/10.1016/j.jclepro.2021.130164>.
- 610 (31) He, S.; Zhu, B.; Jiang, X.; Han, G.; Li, S.; Lau, C. H.; Wu, Y.; Zhang, Y.; Shao, L.  
611 Symbiosis-Inspired de Novo Synthesis of Ultrahigh MOF Growth Mixed Matrix  
612 Membranes for Sustainable Carbon Capture. *Proc. Natl. Acad. Sci. U. S. A.* **2022**, *119* (1),  
613 e2114964119. <https://doi.org/10.1073/pnas.2114964119>.
- 614 (32) Zhu, B.; He, S.; Yang, Y.; Li, S.; Lau, C. H.; Liu, S.; Shao, L. Boosting Membrane  
615 Carbon Capture via Multifaceted Polyphenol-Mediated Soldering. *Nat. Commun.* **2023**  
616 *14* **2023**, *14* (1), 1–9. <https://doi.org/10.1038/s41467-023-37479-9>.
- 617 (33) Ye, Q.; Xu, J. M.; Zhang, Y. J.; Chen, S. H.; Zhan, X. Q.; Ni, W.; Tsai, L. C.; Jiang, T.;  
618 Ma, N.; Tsai, F. C. Metal-Organic Framework Modified Hydrophilic Polyvinylidene  
619 Fluoride Porous Membrane for Efficient Degerming Selective Oil/Water Emulsion  
620 Separation. *npj Clean Water* **2022**, *5* (1), 1–9. [https://doi.org/10.1038/s41545-](https://doi.org/10.1038/s41545-022-00168-z)  
621 [022-00168-z](https://doi.org/10.1038/s41545-022-00168-z).
- 622 (34) Zeng, H.; He, S.; Hosseini, S. S.; Zhu, B.; Shao, L. Emerging Nanomaterial Incorporated  
623 Membranes for Gas Separation and Pervaporation towards Energetic-Efficient  
624 Applications. *Adv. Membr.* **2022**, *2*, 100015–100034.  
625 <https://doi.org/10.1016/j.advmem.2021.100015>.
- 626 (35) Fakhri, H.; Bagheri, H. Two Novel Sets of UiO-66@ Metal Oxide/Graphene Oxide Z-  
627 Scheme Heterojunction: Insight into Tetracycline and Malathion Photodegradation. *J.*  
628 *Environ. Sci.* **2020**, *91*, 222–236. <https://doi.org/10.1016/J.JES.2020.01.013>.

- 629 (36) Du, Q.; Wu, P.; Sun, Y.; Zhang, J.; He, H. Selective Photodegradation of Tetracycline by  
630 Molecularly Imprinted ZnO@NH<sub>2</sub>-UiO-66 Composites. *Chem. Eng. J.* **2020**, *390*,  
631 124614. <https://doi.org/10.1016/J.CEJ.2020.124614>.
- 632 (37) Zhang, R.; Du, B.; Li, Q.; Cao, Z.; Feng, G.; Wang, X.  $\alpha$ -Fe<sub>2</sub>O<sub>3</sub> Nanoclusters Confined  
633 into UiO-66 for Efficient Visible-Light Photodegradation Performance. *Appl. Surf. Sci.*  
634 **2019**, *466*, 956–963. <https://doi.org/10.1016/J.APSUSC.2018.10.048>.
- 635 (38) Ghorbani, M.; Solaimany Nazar, A. R.; Frahadian, M.; Tangestaninejad, S. Fabrication of  
636 Novel ZnO@BiOBr/UiO-66-NH<sub>2</sub> Core-Shell Heterojunction for Improved Tetracycline  
637 Degradation. *Appl. Surf. Sci.* **2023**, *612*, 155819.  
638 <https://doi.org/10.1016/J.APSUSC.2022.155819>.
- 639 (39) Lin, Z.; Wu, Y.; Jin, X.; Liang, D.; Jin, Y.; Huang, S.; Wang, Z.; Liu, H.; Chen, P.; Lv,  
640 W.; Liu, G. Facile Synthesis of Direct Z-Scheme UiO-66-NH<sub>2</sub>/PhC<sub>2</sub>Cu Heterojunction  
641 with Ultrahigh Redox Potential for Enhanced Photocatalytic Cr(VI) Reduction and NOR  
642 Degradation. *J. Hazard. Mater.* **2023**, *443*, 130195–130212.  
643 <https://doi.org/10.1016/J.JHAZMAT.2022.130195>.
- 644 (40) Man, Z.; Meng, Y.; Lin, X.; Dai, X.; Wang, L.; Liu, D. Assembling UiO-66@TiO<sub>2</sub>  
645 Nanocomposites for Efficient Photocatalytic Degradation of Dimethyl Sulfide. *Chem.*  
646 *Eng. J.* **2022**, *431*, 133952–133962. <https://doi.org/10.1016/j.cej.2021.133952>.
- 647 (41) Wei, T.; Zhao, B.; Zhou, Z.; Di, H.; Shumba, T.; Cui, M.; Zhou, Z.; Xu, X.; Qi, M.; Tang,  
648 J.; Ndungu, P. G.; Qiao, X.; Zhang, Z. Removal of Organics and Ammonia in Landfill  
649 Leachate via Catalytic Oxypyrolysis over MOF-Derived Fe<sub>2</sub>O<sub>3</sub>@SiO<sub>2</sub>-Al<sub>2</sub>O<sub>3</sub>. *Sep. Purif.*  
650 *Technol.* **2023**, *305*, 122467. <https://doi.org/10.1016/J.SEPPUR.2022.122467>.
- 651 (42) Nikpour, S.; Ansari-Asl, Z.; Sedaghat, T. Fabrication and Characterization of  
652 Polystyrene/Fe-MOF Composite Beads for Iodine Uptake. *Inorg. Chem. Commun.* **2022**,  
653 *136*, 109141. <https://doi.org/10.1016/J.INOCHE.2021.109141>.
- 654 (43) Li, K.; Zou, S.; Jin, G.; Yang, J.; Dou, M.; Qin, L.; Su, H.; Huang, F. Efficient Removal of  
655 Selenite in Aqueous Solution by MOF-801 and Fe<sub>3</sub>O<sub>4</sub>/MOF-801: Adsorptive Behavior  
656 and Mechanism Study. *Sep. Purif. Technol.* **2022**, *296*, 121384–121400.  
657 <https://doi.org/10.1016/j.seppur.2022.121384>.
- 658 (44) Grad, O.; Dan, M.; Barbu-Tudoran, L.; Tosa, N.; Lazar, M. D.; Blanita, G. MOF/Al<sub>2</sub>O<sub>3</sub>  
659 Composites Obtained by Immobilization of MIL-53(Cr) or MIL-101(Cr) on  $\gamma$ -Alumina:  
660 Preparation and Characterization. *Microporous Mesoporous Mater.* **2023**, *353*, 112518.  
661 <https://doi.org/10.1016/j.micromeso.2023.112518>.
- 662 (45) Cavka, J. H.; Jakobsen, S.; Olsbye, U.; Guillou, N.; Lamberti, C.; Bordiga, S.; Lillerud, K.  
663 P. A New Zirconium Inorganic Building Brick Forming Metal Organic Frameworks with  
664 Exceptional Stability. *J. Am. Chem. Soc.* **2008**, *130* (42), 13850–13851.  
665 [https://doi.org/10.1021/JA8057953/SUPPL\\_FILE/JA8057953\\_SI\\_001.PDF](https://doi.org/10.1021/JA8057953/SUPPL_FILE/JA8057953_SI_001.PDF).
- 666 (46) Winarta, J.; Shan, B.; McIntyre, S. M.; Ye, L.; Wang, C.; Liu, J.; Mu, B. A Decade of  
667 UiO-66 Research: A Historic Review of Dynamic Structure, Synthesis Mechanisms, and  
668 Characterisation Techniques of an Archetypal Metal–Organic Framework. *Cryst. Growth*  
669 *Des.* **2020**, *20* (2), 1347–1362. <https://doi.org/10.1021/acs.cgd.9b00955>.
- 670 (47) Trushina, D. B.; Sapach, A. Y.; Burachevskaia, O. A.; Medvedev, P. V.; Khmelenin, D.

- 671 N.; Borodina, T. N.; Soldatov, M. A.; Butova, V. V. Doxorubicin-Loaded Core–Shell  
672 UiO-66@SiO<sub>2</sub> Metal–Organic Frameworks for Targeted Cellular Uptake and Cancer  
673 Treatment. *Pharmaceutics* **2022**, *14* (7), 1325.  
674 <https://doi.org/10.3390/PHARMACEUTICS14071325/S1>.
- 675 (48) Polshettiwar, V.; Cha, D.; Zhang, X.; Basset, J. M. High-Surface-Area Silica Nanospheres  
676 (KCC-1) with a Fibrous Morphology. *Angew. Chemie - Int. Ed.* **2010**, *49* (50), 9652–9656.  
677 <https://doi.org/10.1002/anie.201003451>.
- 678 (49) Singh, R.; Bapat, R.; Qin, L.; Feng, H.; Polshettiwar, V. Atomic Layer Deposited (ALD)  
679 TiO<sub>2</sub> on Fibrous Nano-Silica (KCC-1) for Photocatalysis: Nanoparticle Formation and  
680 Size Quantization Effect. *ACS Catal.* **2016**, *6* (5), 2770–2784.  
681 <https://doi.org/10.1021/acscatal.6b00418>.
- 682 (50) Bayal, N.; Singh, R.; Polshettiwar, V. Nanostructured Silica–Titania Hybrid Using  
683 Dendritic Fibrous Nanosilica as a Photocatalyst. *ChemSusChem* **2017**, *10* (10), 2182–  
684 2191. <https://doi.org/10.1002/cssc.201700135>.
- 685 (51) Bayal, N.; Singh, B.; Singh, R.; Polshettiwar, V. Size and Fiber Density Controlled  
686 Synthesis of Fibrous Nanosilica Spheres (KCC-1). *Sci. Rep.* **2016**, *6* (1), 1–11.  
687 <https://doi.org/10.1038/srep24888>.
- 688 (52) Douglas C. Montgomery. *Design and Analysis of Experiments, 10th Edition* / Wiley; 2019.
- 689 (53) Le, X.; Dong, Z.; Li, X.; Zhang, W.; Le, M.; Ma, J. Fibrous Nano-Silica Supported  
690 Palladium Nanoparticles: An Efficient Catalyst for the Reduction of 4-Nitrophenol and  
691 Hydrodechlorination of 4-Chlorophenol under Mild Conditions. *Catal. Commun.* **2015**,  
692 *59*, 21–25. <https://doi.org/10.1016/j.catcom.2014.09.029>.
- 693 (54) Makuła, P.; Pacia, M.; Macyk, W. How To Correctly Determine the Band Gap Energy of  
694 Modified Semiconductor Photocatalysts Based on UV-Vis Spectra. *J. Phys. Chem. Lett.*  
695 **2018**, *9* (23), 6814–6817.  
696 [https://doi.org/10.1021/ACS.JPCLETT.8B02892/SUPPL\\_FILE/JZ8B02892\\_LIVESLIDE](https://doi.org/10.1021/ACS.JPCLETT.8B02892/SUPPL_FILE/JZ8B02892_LIVESLIDE)  
697 S.MP4.
- 698 (55) Dong, F.; Wang, Z.; Li, Y.; Ho, W. K.; Lee, S. C. Immobilization of Polymeric G-C<sub>3</sub>N<sub>4</sub>  
699 on Structured Ceramic Foam for Efficient Visible Light Photocatalytic Air Purification  
700 with Real Indoor Illumination. *Environ. Sci. Technol.* **2014**, *48* (17), 10345–10353.  
701 <https://doi.org/10.1021/es502290f>.
- 702 (56) Zhang, Y.; Zhou, J.; Feng, Q.; Chen, X.; Hu, Z. Visible Light Photocatalytic Degradation  
703 of MB Using UiO-66/g-C<sub>3</sub>N<sub>4</sub> Heterojunction Nanocatalyst. *Chemosphere* **2018**, *212*,  
704 523–532. <https://doi.org/10.1016/J.CHEMOSPHERE.2018.08.117>.
- 705 (57) Kubra, K. T.; Hasan, M. M.; Hasan, M. N.; Salman, M. S.; Khaleque, M. A.; Sheikh, M.  
706 C.; Rehan, A. I.; Rasee, A. I.; Waliullah, R. M.; Awual, M. E.; Hossain, M. S.; Alsukaibi,  
707 A. K. D.; Alshammari, H. M.; Awual, M. R. The Heavy Lanthanide of Thulium(III)  
708 Separation and Recovery Using Specific Ligand-Based Facial Composite Adsorbent.  
709 *Colloids Surfaces A Physicochem. Eng. Asp.* **2023**, *667*, 131415.  
710 <https://doi.org/10.1016/j.colsurfa.2023.131415>.
- 711 (58) Brunauer, S.; Emmett, P. H.; Teller, E. Adsorption of Gases in Multimolecular Layers. *J.*  
712 *Am. Chem. Soc.* **1938**, *60* (2), 309–319. <https://doi.org/10.1021/ja01269a023>.

- 713 (59) Ambroz, F.; Macdonald, T. J.; Martis, V.; Parkin, I. P. Evaluation of the BET Theory for  
714 the Characterization of Meso and Microporous MOFs. *Small Methods* **2018**, *2* (11),  
715 1800173. <https://doi.org/10.1002/smt.201800173>.
- 716 (60) Awual, M. R.; Rahman, I. M. M.; Yaita, T.; Khaleque, M. A.; Ferdows, M. PH Dependent  
717 Cu(II) and Pd(II) Ions Detection and Removal from Aqueous Media by an Efficient  
718 Mesoporous Adsorbent. *Chem. Eng. J.* **2014**, *236*, 100–109.  
719 <https://doi.org/10.1016/j.cej.2013.09.083>.
- 720 (61) Hasan, M. N.; Salman, M. S.; Hasan, M. M.; Kubra, K. T.; Sheikh, M. C.; Rehan, A. I.;  
721 Rasee, A. I.; Awual, M. E.; Waliullah, R. M.; Hossain, M. S.; Islam, A.; Khandaker, S.;  
722 Alsukaibi, A. K. D.; Alshammari, H. M.; Awual, M. R. Assessing Sustainable  
723 Lutetium(III) Ions Adsorption and Recovery Using Novel Composite Hybrid  
724 Nanomaterials. *J. Mol. Struct.* **2023**, *1276*, 134795.  
725 <https://doi.org/10.1016/j.molstruc.2022.134795>.
- 726 (62) Salman, M. S.; Hasan, M. N.; Hasan, M. M.; Kubra, K. T.; Sheikh, M. C.; Rehan, A. I.;  
727 Waliullah, R. M.; Rasee, A. I.; Awual, M. E.; Hossain, M. S.; Alsukaibi, A. K. D.;  
728 Alshammari, H. M.; Awual, M. R. Improving Copper(II) Ion Detection and Adsorption  
729 from Wastewater by the Ligand-Functionalized Composite Adsorbent. *J. Mol. Struct.*  
730 **2023**, *1282*, 135259. <https://doi.org/10.1016/j.molstruc.2023.135259>.
- 731 (63) Hasan, M. M.; Kubra, K. T.; Hasan, M. N.; Awual, M. E.; Salman, M. S.; Sheikh, M. C.;  
732 Rehan, A. I.; Rasee, A. I.; Waliullah, R. M.; Islam, M. S.; Khandaker, S.; Islam, A.;  
733 Hossain, M. S.; Alsukaibi, A. K. D.; Alshammari, H. M.; Awual, M. R. Sustainable  
734 Ligand-Modified Based Composite Material for the Selective and Effective Cadmium(II)  
735 Capturing from Wastewater. *J. Mol. Liq.* **2023**, *371*, 121125.  
736 <https://doi.org/10.1016/j.molliq.2022.121125>.
- 737 (64) Aghajanzadeh, M.; Zamani, M.; Molavi, H.; Khieri Manjili, H.; Danafar, H.; Shojaei, A.  
738 Preparation of Metal–Organic Frameworks UiO-66 for Adsorptive Removal of  
739 Methotrexate from Aqueous Solution. *J. Inorg. Organomet. Polym. Mater.* **2018**, *28* (1),  
740 177–186. <https://doi.org/10.1007/s10904-017-0709-3>.
- 741 (65) Du, X.; He, J. Fine-Tuning of Silica Nanosphere Structure by Simple Regulation of the  
742 Volume Ratio of Cosolvents. *Langmuir* **2010**, *26* (12), 10057–10062.  
743 [https://doi.org/10.1021/LA100196J/SUPPL\\_FILE/LA100196J\\_SI\\_001.PDF](https://doi.org/10.1021/LA100196J/SUPPL_FILE/LA100196J_SI_001.PDF).
- 744 (66) Duma, Z. G.; Dyosiba, X.; Moma, J.; Langmi, H. W.; Louis, B.; Parkhomenko, K.;  
745 Musyoka, N. M. Thermocatalytic Hydrogenation of CO<sub>2</sub> to Methanol Using Cu-ZnO  
746 Bimetallic Catalysts Supported on Metal–Organic Frameworks. *Catalysts* **2022**, *12* (4),  
747 401–416. <https://doi.org/10.3390/catal12040401>.
- 748 (67) Wang, J.; He, Y.; Wan, X.; Xie, F.; Sun, Y.; Li, T.; Xu, Q.; Zhao, D.; Qu, Q. Core-Shell  
749 Metal-Organic Framework/Silica Hybrid with Tunable Shell Structure as Stationary Phase  
750 for High Performance Liquid Chromatography. *J. Chromatogr. A* **2023**, *1705*, 464164.  
751 <https://doi.org/10.1016/j.chroma.2023.464164>.
- 752 (68) Bouhrara, M.; Ranga, C.; Fihri, A.; Shaikh, R. R.; Sarawade, P.; Emwas, A. H.; Hedhili,  
753 M. N.; Polshettiwar, V. Nitridated Fibrous Silica (KCC-1) as a Sustainable Solid Base  
754 Nanocatalyst. *ACS Sustain. Chem. Eng.* **2013**, *1* (9), 1192–1199.  
755 <https://doi.org/10.1021/sc400126h>.



- 756 (69) Cao, Z.; Zhang, T.; Ren, P.; Cao, D.; Lin, Y.; Wang, L.; Zhang, B.; Xiang, X. Doping of  
757 Chlorine from a Neoprene Adhesive Enhances Degradation Efficiency of Dyes by  
758 Structured TiO<sub>2</sub>-Coated Photocatalytic Fabrics. *Catalysts* **2020**, *10* (1), 69–85.  
759 <https://doi.org/10.3390/catal10010069>.
- 760 (70) Li, S.; Hu, C.; Peng, Y.; Chen, Z. One-Step Scalable Synthesis of Honeycomb-like g-  
761 C<sub>3</sub>N<sub>4</sub> with Broad Sub-Bandgap Absorption for Superior Visible-Light-Driven  
762 Photocatalytic Hydrogen Evolution. *RSC Adv.* **2019**, *9* (56), 32674–32682.  
763 <https://doi.org/10.1039/c9ra07068k>.
- 764 (71) Delekar, S. D.; Dhodamani, A. G.; More, K. V.; Dongale, T. D.; Kamat, R. K.; Acquah, S.  
765 F. A.; Dalal, N. S.; Panda, D. K. Structural and Optical Properties of Nanocrystalline TiO<sub>2</sub>  
766 with Multiwalled Carbon Nanotubes and Its Photovoltaic Studies Using Ru(II) Sensitizers.  
767 *ACS Omega* **2018**, *3* (3), 2743–2756. <https://doi.org/10.1021/acsomega.7b01316>.
- 768 (72) Zhao, J.; Hidaka, H.; Takamura, A.; Pelizzetti, E.; Serpone, N. Photodegradation of  
769 Surfactants. 11.  $\zeta$ -Potential Measurements in the Photocatalytic Oxidation of Surfactants  
770 in Aqueous TiO<sub>2</sub> Dispersions. *Langmuir* **1993**, *9* (7), 1646–1650.  
771 [https://doi.org/10.1021/LA00031A008/ASSET/LA00031A008.FP.PNG\\_V03](https://doi.org/10.1021/LA00031A008/ASSET/LA00031A008.FP.PNG_V03).
- 772 (73) Mohammadi, A.; Pourmoslemi, S. Enhanced Photocatalytic Degradation of Doxycycline  
773 Using a Magnetic Polymer-ZnO Composite. *Water Sci. Technol.* **2018**, *2017* (3), 791–801.  
774 <https://doi.org/10.2166/wst.2018.237>.
- 775 (74) Li, D.; Hua, T.; Li, X.; Cheng, J.; Du, K.; Hu, Y.; Chen, Y. In-Situ Fabrication of Ionic  
776 Liquids/MIL-68(In)-NH<sub>2</sub> Photocatalyst for Improving Visible-Light Photocatalytic  
777 Degradation of Doxycycline Hydrochloride. *Chemosphere* **2022**, *292*, 133461.  
778 <https://doi.org/10.1016/j.chemosphere.2021.133461>.
- 779 (75) Mehrotra, K.; Yablonsky, G. S.; Ray, A. K. Kinetic Studies of Photocatalytic Degradation  
780 in a TiO<sub>2</sub> Slurry System: Distinguishing Working Regimes and Determining Rate  
781 Dependences. *Ind. Eng. Chem. Res.* **2003**, *42* (11), 2273–2281.  
782 <https://doi.org/10.1021/IE0209881>.
- 783 (76) Chen, Z.; Ou, D.; Gu, G.; Gao, S.; Li, X.; Hu, C.; Liang, X.; Zhang, Y. Removal of  
784 Tetracycline from Water by Catalytic Photodegradation Combined with the Microalga  
785 *Scenedesmus Obliquus* and the Responses of Algal Photosynthesis and Transcription. *J.*  
786 *Environ. Manage.* **2023**, *326*, 116693. <https://doi.org/10.1016/J.JENVMAN.2022.116693>.
- 787 (77) Han, W.; Shou, J.; Yang, Y.; Chen, L.; Zhang, L.; Chen, Y.; Tu, X.; Jin, D.; Zhang, S.;  
788 Chang, Y.; Zheng, H. High-Efficient Removal of Tetracycline in Water via Porous  
789 Magnetic Ce/Fe Photocomposite under Visible Light. *J. Rare Earths* **2022**.  
790 <https://doi.org/10.1016/J.JRE.2022.07.015>.
- 791 (78) Rahman, N.; Raheem, A. Graphene Oxide/Mg-Zn-Al Layered Double Hydroxide for  
792 Efficient Removal of Doxycycline from Water: Taguchi Approach for Optimization. *J.*  
793 *Mol. Liq.* **2022**, *354*, 118899. <https://doi.org/10.1016/J.MOLLIQ.2022.118899>.
- 794 (79) Srivastava, A.; Dave, H.; Prasad, B.; Maurya, D. M.; Kumari, M.; Sillanpää, M.; Prasad,  
795 K. S. Low Cost Iron Modified Syzygium Cumini l. Wood Biochar for Adsorptive  
796 Removal of Ciprofloxacin and Doxycycline Antibiotics from Aqueous Solution. *Inorg.*  
797 *Chem. Commun.* **2022**, *144*, 109895–109904.

798 <https://doi.org/10.1016/J.INOCHE.2022.109895>.

799 (80) Tian, Y.; Liu, F.; Sun, B.; Tong, Z.; Fu, P.; Zhang, J.; Bi, W.; Xu, S.; Pei, G. Efficient  
800 Removal of Doxycycline Using Schwertmannite as a Heterogeneous Fenton-like Catalyst  
801 over a Wide PH Range. *J. Environ. Chem. Eng.* **2023**, *11* (2), 109441.  
802 <https://doi.org/10.1016/j.jece.2023.109441>.

803

804

805

806

807

808

809

810

811

812

813

814

815

816

817

818

819

820

821

822

823

824

825

826

827

828

829

830

